Spring 2022

Effects of vacancies and electron temperature on the electron phonon coupling in cubic silicon carbide and their connection to the inelastic thermal spike

Salah Al-Smairat

Department: Nuclear Engineering and Radiation Science

EFFECTS OF VACANCIES AND ELECTRON TEMPERATURE ON THE ELECTRON PHONON COUPLING IN CUBIC SILICON CARBIDE AND THEIR CONNECTION TO THE INELASTIC THERMAL SPIKE

by

SALAH ABDUL-RAHAMAN AL-SMAIRAT

A DISSERTATION

Presented to the Graduate Faculty of the

MISSOURI UNIVERSITY OF SCIENCE AND TECHNOLOGY

In Partial Fulfillment of the Requirements for the Degree

DOCTOR OF PHILOSOPHY

in

NUCLEAR ENGINEERING

2022

Approved by:

Joseph Graham, Advisor
Muthanna Al-Dahhan
Ayodeji B. Alajo
Carlos H. Castaño Giraldo
Aleksandr Chernatynskiy

PUBLICATION DISSERTATION OPTION

This dissertation consists of the following two manuscripts, formatted in the style used by the Missouri University of Science and Technology:

Paper I, found on pages 33–60, has been published in *Journal of Applied Physics.*

Paper II, found on pages 61–73, was submitted to *Nuclear Instruments and Methods in Physics Research B.*

ABSTRACT

The electron-phonon interaction is an important interaction in many solids as it influences transport phenomena and related quantities such as the electrical and thermal conductivities, especially in nuclear and space applications. The importance of the electron-phonon interaction in primary damage production in 3C-SiC is the subject of this research.

The electron-phonon coupling factor was calculated using a hybrid Density Functional Perturbation Theory – Classical Electron Gas model. The coupling factor was calculated as a function of electron temperature in pristine and defective 3C-SiC, and relaxed defective cells. The electron-phonon coupling is found to depend strongly on the electronic temperature and on the presence of vacancies. Electron-phonon mean free paths were calculated to explore the possibility of extending those calculations to lower vacancy concentrations using a rule-of-mixtures approach.

The electron-temperature-dependent couplings were implemented in the Two-Temperature Model (TTM), which was used to model the evolution of electron and phonon temperatures following impact from a Swift Heavy Ion. Those results were compared to similar calculations using constant coupling values. The use of a constant coupling is justifiable at lower electronic stopping powers far from the track core (beyond several nm). At the center of the track, however, the coupling is strong (on the order of 10^{16} W cm^{-3} K) and decreases rapidly with radius. These results reveal some weaknesses of the TTM model and indicate that near the track core, the assumption of quasi-thermal equilibrium is not necessarily valid at high electronic excitation densities.

ACKNOWLEDGMENTS

I would like to acknowledge my supervisor, Dr. Joseph Graham. No words would be enough to express my gratitude for his kind, professional, experienced supervision. Without his knowledge and support, my research would not have seen the light. Also, I would like to express my gratitude to my dissertation committee for their dedication and time. I thank the Information Technology teams of the Missouri University of Science and Technology and the University of Missouri-Columbia for their help and support in using the computing clusters on both campuses. My thanks goes out to all staff and faculty in the Nuclear Engineering and Radiation Science Department, especially the professors for their help, support, and kindness.

I would be neglectful if I did not thank Dr. Mohammad Aljohani, my former chairman for his motivation and support. Without Dr. Aljohani's help and motivation, I would not have been started my Ph.D. I would like to thank fellow students, friends, and everyone who has helped me during my research journey.

My dear parents, thank you for your unlimited and unconditional love and support. You were the candle in the darkest moment in my life. Deep thanks to my brothers and sisters and the whole family. Finally, I thank my wife and my children for their patience, support, and love. You are the soul of my life. I love you all.

TABLE OF CONTENTS

Page

LIST OF ILLUSTRATIONS

SECTION Page

1. INTRODUCTION

1.1. SILICON CARBIDE (SiC)

SiC is a high temperature ceramic and wide bandgap semiconductor with outstanding mechanical and physiochemical properties that make it useful in many fields of industry and technology. Its high hardness (9 Mohs scale), low thermal expansion coefficient (4×10^{-6} K^{-1}), good chemical stability, high thermal conductivity (>60 W m^{-1} K^{-1}), high melting temperature (2730 °C), and radiation tolerance are all strongly desirable properties for a material subject to extreme conditions found in manufacturing, the aerospace industry, high power electronics, and nuclear applications. In the nuclear power industry, SiC is used as a structural material and a component of nuclear fuel.

SiC is used as a coating in Tri-Isostructural (TRISO) particles, a mature fuel technology that has been employed in high-temperature gas-cooled reactors (HTGR)[1] . More recently, SiC has been considered as a coating for structural materials and flow channels in fusion reactors , in heat exchangers in HTGRs, and in control rods and core structures in light water reactors [2]. There have been efforts led by companies in the nuclear industry such as General Atomics, Westinghouse, and Framatome/Areva to replace zirconium alloy cladding with SiC [3]. In the years following the Fukushima-Daichi event of 2011, the nuclear industry started making a strong effort to enhance the accident tolerance of light water reactors (LWRs) and their fuels. Particular attention has been placed on replacing zirconium alloys - which can oxidize rapidly in high temperature steam, producing explosive hydrogen - with a more chemically inert, yet strong, fuel cladding [4]. In addition to the properties above, SiC has good oxidation

resistance at high temperatures, minimizing hydrogen production, and a very high sublimation temperature making SiC one of main candidate materials in accident tolerant fuel cladding [5].

In addition to its high temperature strength and chemical durability, SiC has intriguing electrical properties. In the aerospace and electronics industries, SiC is used in light-emitting diodes, high power devices, microwave devices, among others [6]. SiC, being composed of two abundant and non-toxic elements, is biocompatible and environmentally friendly. Indeed, SiC has been considered as a suitable substitute for certain noble metals, and rare-earth elements in some applications [7].

SiC is a covalently bonded material composed of SiC_4 tetrahedra arranged in a number of polytypes, which can be uniquely identified by their stacking sequence. There are more than 250 polytypes or polymorphs for SiC. It is common to refer to the cubic polytype, 3C-SiC, as β-SiC and the tremendous number of non-cubic polytypes (hexagonal and rhombohedral) collectively as α-SiC. The cubic polytype, 3C-SiC, which will be the focus of this work, is shown in Figure 1.1. 3C-SiC has a cubic zincblende structure.

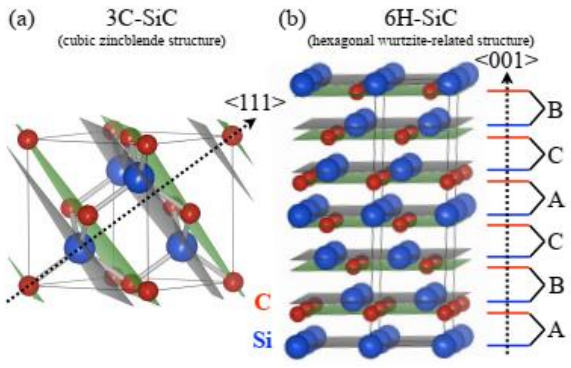

Figure 1.1: Unit Cell Structures illustration (a) 3C-SiC unit cell (b) 6H-SiC unit cell [8]

1.2. RADIATION EFFECTS IN SIC

Particle radiation can be divided into two types. *Non-ionizing* radiations (e.g. radio waves, microwaves, visible light) do not have sufficient energy to remove an electron from an atom but nonetheless can carry energy through space. Ionizing radiation, on the other hand, can excite or ionize atoms and molecules, temporarily or permanently modifying the electronic structure of the material. In living tissue, this poses a well-known health risk. In materials used in industrial and technological applications, properties can be altered, sometimes in dramatic ways.

Commonly encountered ionizing radiations in nuclear applications include alpha particles, beta particles, X-rays, γ-rays, neutrons, and swift ions. The energy transfer from each particle type in matter depends on the particle's mass, charge, energy, and its specific interactions with the electrons and nuclei that make up the material. For example, γ-ray photons can interact with orbital electrons through the photoelectric effect, Compton scattering, and pair production, while neutrons interact directly with the nucleus through elastic scattering, inelastic scattering, and absorption reactions. The focus of this research will be on energetic charged particles which interact with both the electrons and nuclei through the Coulomb force, with particular attention paid to swift heavy ions (SHI). Swift heavy ions are heavier than carbon and possess a specific kinetic energy of 1 MeV/u or greater[9]. An important example of swift heavy ions are the energetic fission fragments produced through nuclear fission reactions.

When swift heavy ions interact with matter, they transfer kinetic energy to electrons through the Coulomb interaction, generating high energy electrons, so-called delta electrons, and exciting lower energy plasmons, collective charge density

oscillations. After a short time, the excited electronic system thermalizes in what is termed the inelastic *thermal spike* and a hot electron plasma is formed (or electron-hole plasma in the case of band-gap materials). The situation is illustrated in Figure 1.2. As the plasma cools, it couples to the atomic lattice, transferring energy in the process and heating the lattice. A central parameter governing the energy transfer is the electron-phonon coupling. It describes the strength of the interaction processes where energy is transferred between electrons and phonons, quanta of lattice vibrations. Its strength determines the rate of lattice heating, and therefore the maximum temperatures reached in the vicinity of the ion trajectory.

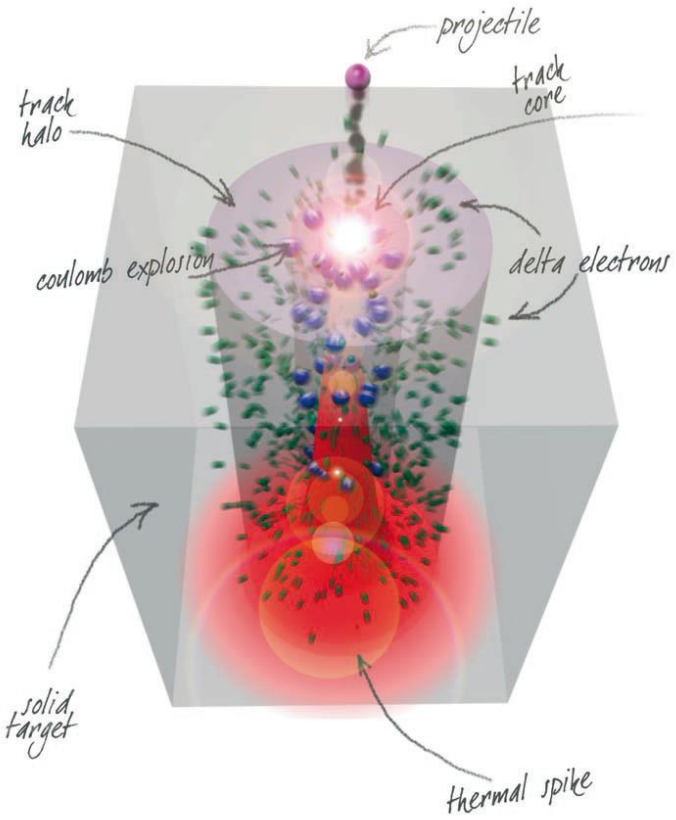

Figure 1.2: Swift heavy ion interaction with matter [10]

One of the most striking effects of this process is the formation of *ion tracks*, regions of amorphous or highly disordered material embedded in a crystalline matrix. Experiments and models show that a useful criterion for predicting if tracks will form is whether the maximum lattice temperature exceeds the melting point of the material. When it does, a column of molten material can form. As the track cools, an amorphous or highly defective region can remain. On the other hand, partial or total recrystallization has been observed in some materials[11]. It is evident that particle stopping power, electron-phonon coupling, melting point, heat capacity, and lattice thermal conductivity are all important parameters in determining ion track structure. This thesis will focus on one of these aspects of the ion matter interaction, namely, the electron-phonon coupling.

1.3. RESEARCH SCOPE AND CONTRIBUTIONS

This thesis explores three different aspects of the electron-phonon coupling in 3C-SiC. First, the electronic temperature-dependence of the coupling is calculated. Second, the modulation of the coupling by lattice defects is investigated. Finally, we study the consequences of using a temperature-variable coupling in the so-called *two temperature model*. The two-temperature model (TTM) is a commonly used model to explain ion track formation in a variety of materials. Virtually all calculations published using the two-temperature model assume a constant electron-phonon coupling. We will show that this assumption can be partially justified in some cases but not in others. In certain circumstances the temperature-variable coupling leads to qualitatively and quantitatively different behavior. Indeed, a key conclusion of this work is that the electron-phonon coupling is non-uniform in the track and the rate of energy transfer in the center of the

track is so rapid at high electronic excitation densities, that the assumption of well-defined electron and phonon temperatures breaks down.

This work proceeds through a method of calculating the electron-phonon coupling (EPC) for 3C-SiC using density functional perturbation theory (DFPT) as a function of electron temperature. Because band structure calculations are not well suited to the higher extremes of electronic temperatures, a hybrid model, which treats highly excited electrons as a classical gas, is used to extend the calculation to temperatures above 10,000 K. The results indicate that the coupling constant increases dramatically with electronic temperature. This may be a general feature of semiconductors and insulators. The coupling in metals has a comparatively weak temperature dependence.

The effect of structural defects on the coupling constant is studied by introducing carbon and silicon vacancies into a supercell. A code was developed for solving the two-temperature model (TTM) equations with a temperature-dependent coupling constant. Results of the calculation using a variable coupling were compared with those obtained using different values of constant couplings. A result of the strong temperature dependence is a similarly strong radial dependence of the coupling strength. The results may help in understanding the effect of annealing of preexisting defects in highly defective SiC. They also call into question the validity of the assumption of well-defined electron and phonon temperatures over the entire track. For insulators and semiconductors, it may eventually become necessary to consider three temperatures, one for electrons, one for holes, and one for the lattice, with an additional conservation equation governing the number of electrons and holes.

2. STATE OF KNOWLEDGE

2.1. SILICON CARBIDE: PROPERTIES AND USES

Silicon carbide, or carborundum, is a non-oxide ceramic that has been an industrially and commercially important material since the 1800s, when it was first used as an abrasive. Since then, it has entered a diverse variety of applications which make use of its desirable mechanical, thermal and electrical properties. Although it is rarely found in its natural form (the mineral moissanite), it can be synthesized commercially. There are about 250 crystal structures of SiC. The fundamental unit of these structures is the covalently bonded SiC_4 (or CSi_4) tetrahedron [7]. Thus, all polytypes have the same short-range order up to nearest neighbor. The rest of the structure is determined by stacking sequence. The SiC polytypes can be visualized as stacked Si-C double atomic layers. Each Si-C double atomic layer is composed of parallel monolayers of Si or C atoms bonded by Si-C covalent bonds oriented perpendicular to the planes along a high symmetry axis (conventionally designated the c-axis). One orientation of the layer is denoted the A layer. Translation of the A layer yields a B layer. The addition of a 60° rotation about the c-axis gives a C layer. Different stacking sequences of A, B, and C layers describe the multitudes of polytypes. Figure 2.1 shows the stacking sequences of the 6H, 4H, and 3C polytypes. 3C-SiC is formed by the ABCABC stacking sequence. The tetrahedral coordination can be readily seen in Figure 1.1.

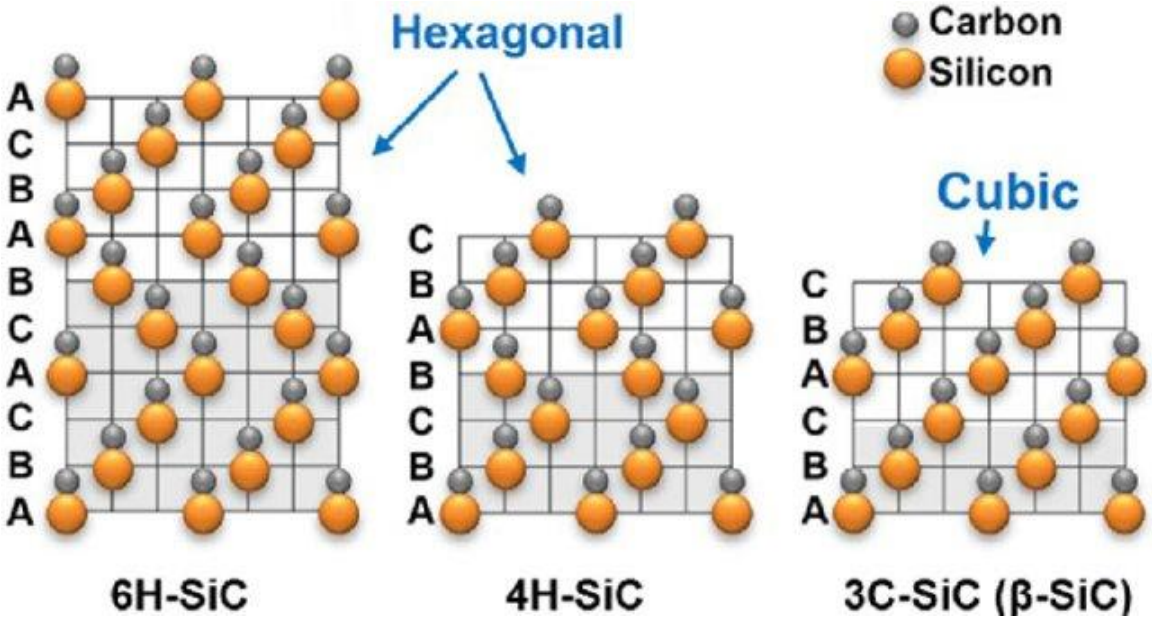

Figure 2.1: Stacking sequence of the 6H-, 4H-, and 3C-SiC polytypes[12]

Cubic SiC is also referred to as β-SiC to distinguish from and the hexagonal and rhombohedral polytypes, referred to collectively as α-SiC. Some properties, such as density, elastic modulus, and coefficient of thermal expansion are similar for all polytypes, owing to similar short-range order and bonding. Other properties, which depend to a greater extent on lattice symmetry and long-range order, can show stronger variations across polytype. For example, the indirect band gap for 3C-SiC is 2.4 eV, while the band gap is somewhat higher, 2.9-3.3 eV, for hexagonal structures [13]

Because of its wear resistance, high temperature strength, and semiconducting properties, SiC is used in automotive engines, heat exchangers, high-temperature bearings, heavy-duty electric contacts, high temperature fixtures, nozzles, turbine blades, and stators [14]. Figure 2.2 illustrates some of the power-related products of SiC and their market share.

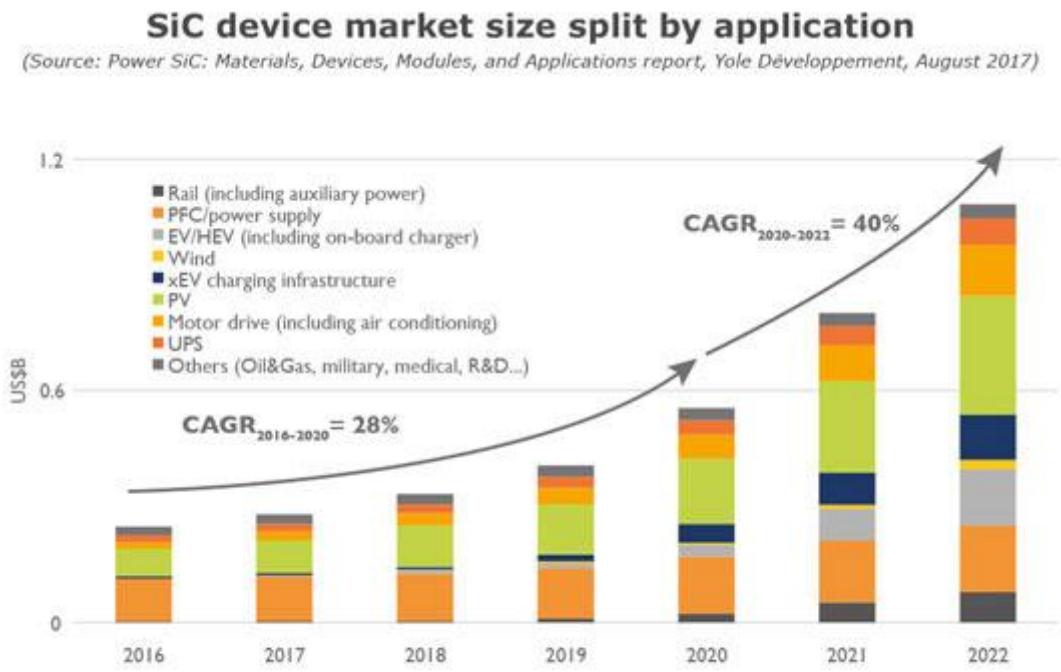

Figure 2.2: Some of SiC products and their market share [15]

In the nuclear power industry, SiC has been long considered an advanced material capable of withstanding the extremes of temperature and radiation damage found in fission and fusion reactors. One of the most mature nuclear technologies incorporating SiC is in the fuel for High Temperature Gas Reactors (HTGRs).

HTGRs utilize microsphere tristructural-isotropic (TRISO) fuel particles embedded in a graphite matrix, taking either the form of a pebble or a monolithic compact. The fuel particles, about 1 mm in diameter, have a layered structure comprised of a central fuel kernel (oxide, carbide, or oxycarbide ceramic), coated by a low-density carbonaceous buffer layer, followed by layers of inner pyrolytic carbon (IPyC), silicon

carbide (SiC), and an outer shell of pyrolytic carbon (OPyC). A TRISO particle is shown in Figure 2.3.

The role of the SiC layer in TRISO particles is to act as a “miniature containment vessel.” The SiC layer provides mechanical strength, crush resistance, dimensional stability, and, having low atomic diffusion coefficients, it acts as an effective fission product barrier. Thus, the SiC layer, rather than cladding, becomes the primary fission product barrier that contains the fission products. It also keeps chlorine and hydrochloric acid, reagents used in the fuel fabrication process, from permeating and chemically attacking the fuel kernel [16].

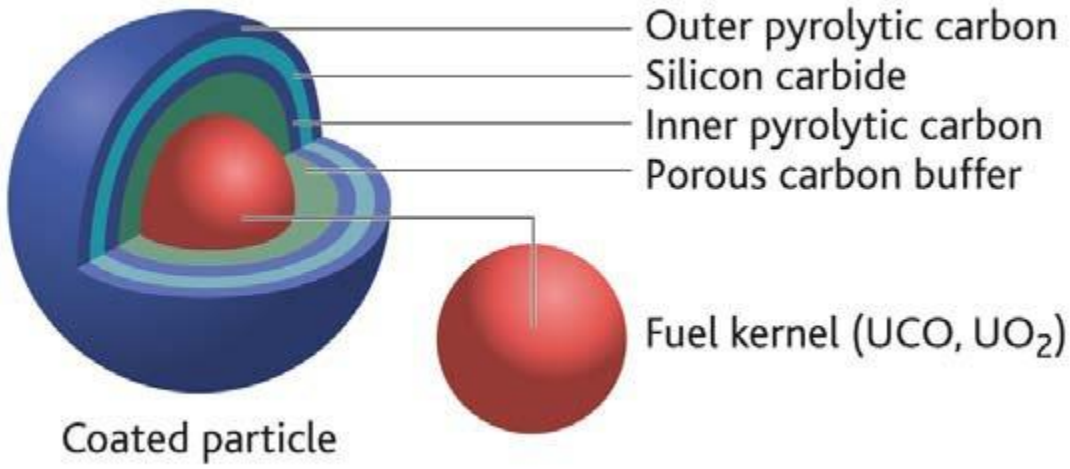

Figure 2.3: Tri-Isostructural (TRISO) fuel particle[17]

The TRISO concept was originally developed for HTGRs but it has more recently been considered as a replacement for standard oxide fuel in commercial light water

reactors (LWRs), and as fuel in fluoride salt cooled reactors [18]. Figure 2.4 shows how TRISO fuel could be adapted to the LWR fuel form factor.

Figure 2.4: Use of TRISO in light water reactor (LWR) fuel[18]

Silicon carbide has been identified as a robust material in several other nuclear power applications. Self-sufficient magnetic confinement DT fusion reactors incorporate a tritium breeding blanket just outside the first wall of the vacuum vessel. The breeding blanket in a hypothetical commercial fusion reactor will have to withstand 15-30 displacements per atom (dpa) per year of radiation damage, under nearly continuous operation. SiC fiber-reinforced SiC-matrix (SiCf/SiC) composite is a candidate structural material for such a blanket in the Demonstration fusion reactor (DEMO) [19].

In HTGRs, intermediate heat exchangers are required to withstand temperatures of ~1000 °C. SiCf/SiC has been considered as an alternative to metal alloys because of its

high temperature strength, microstructural stability, chemical stability, and thermal performance[20] [2].

2.2. RADIATION INTERACTIONS WITH MATTER

The focus of this thesis is on primary radiation effects of energetic charged particles, with particular attention paid to swift ions. In the context of nuclear energy, energetic ions appear from several interactions. Fission spectrum and fusion neutrons can generate swift light ions (isotopes of H and He) through a number of threshold direct reactions (e.g. (n,p), (n,t), (n,nα)). Neutron elastic and inelastic scattering from fast or fusion neutrons produce primary knock-on atoms (recoil nuclei), medium energy ions with up to tens or hundreds of keV of energy, depending on target material. Swift heavy ions, ions having a specific kinetic energy greater than 1 MeV/u and masses greater than 4 amu, include many fission fragments. In aerospace contexts, swift heavy ions also appear in the form of solar ions and galactic cosmic rays.

The interaction of energetic ions with matter is important in several respects. In a health physics and radiological protection context, swift ions are the most biologically destructive of the nuclear radiations. In spacecraft, solar ions and galactic cosmic rays represent a major concern as performance and reliability of electronics and sensors can be greatly affect by those radiations. On manned space missions, acute radiation dose rates to astronauts from solar storms is a common hazard[21]. On interplanetary missions (e.g. Earth to Mars transit) accumulated dose rates are a significant consideration as the Earth's magnetosphere no longer protects astronauts from galactic cosmic rays. In the nuclear industry, radiation damage from charged particle affects numerous aspects of

materials performance in nuclear reactors. Damage to the fuel from fission products produce some of the most radical microstructural and property changes of any material in the reactor core.

2.3. ENERGY LOSS BY CHARGED PARTICLES

As a charged particle penetrates a material, it losses energy to orbital electrons through the Coulomb interaction and to nuclei through the Coulomb interaction or direct interactions. The rate of energy loss is described by the stopping power. The electronic stopping power (S_e), is the rate of energy loss through electronic excitation and ionization per unit distance that the particle travels. Similarly, nuclear stopping power (S_n) is the rate of energy loss through discrete particle-nucleus collisions per unit distance traveled. For ions, the total stopping power is essentially the sum of the two. For electrons and positrons where energy loss through Bremsstrahlung can occur, a radiative stopping is also included. In the high velocity/high energy limit, the electronic stopping power is given by the relativistic Bethe formula

$$-\frac{dE}{dx} = \frac{4\pi k^2 Z^2 e^4 n}{c^2 \beta^2}\left[\ln\frac{2mc^2\beta^2}{I(1-\beta^2)} - \beta^2\right] \quad (1)$$

k is the electric constant (8.99×10^8 N m^2 C^{-2}), Z is the charge number (atomic number for ions), e is fundamental electric charge, $\beta = \frac{v}{c}$ is the particle speed, I is the mean excitation potential, and n is the electron density. At energy ranges where the Bethe formula is valid, the nuclear stopping is small and usually neglected.

While the Bethe formula is quantitatively accurate for swift protons and alpha particles and relativistic ions, slower, heavier ions face several additional effects

including charge screening, the shell correction, the Barkas-Anderson effect (order Z^3 correction), and the Bloch-correction (order Z^4 correction). These among other features, these give rise to the appearance of Bragg peak, a maximum in the stopping power. For energies below the Bragg peak, the electronic stopping power decreases towards zero. At the same time the nuclear stopping power becomes significant at low energies and can dominate the energy loss process. Thus for energetic ions nuclear stopping is thought of as a low energy process while electronic stopping is a high energy process [22]. Figure 2.5 illustrates the energy dependence of electronic and nuclear stopping powers. The maximum in the electronic stopping power corresponds to the Bragg peak.

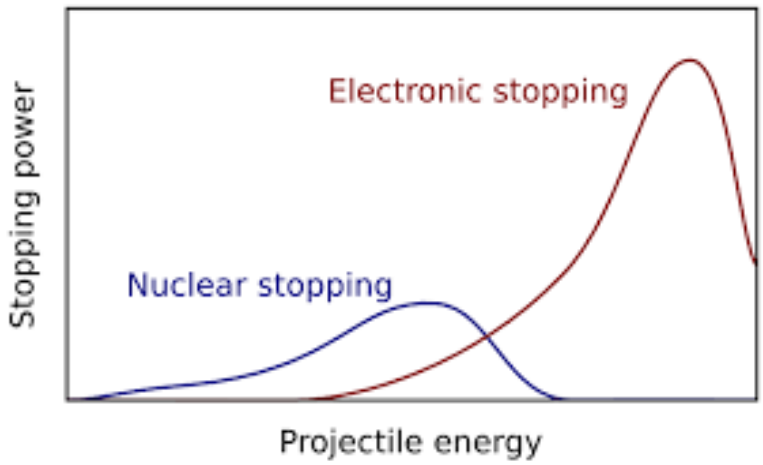

Figure 2.5: Illustration of electronic and nuclear stopping power [22]

In the nuclear energy loss regime, heavy ions produce structural modifications to the lattice occur through displacement cascades. Displacement cascades, a sequence of binary atom collisions generating primary and secondary knock-on atoms, have the ability to generate large numbers of point defects (vacancies and self-interstitial atoms),

defect clusters, and through subsequent defect interactions, extended defects [23]. At low temperatures, displacement cascades can form amorphous zone.

In the electronic energy loss regime, bond breaking and production of large densities of electron holes pairs occurs. Subsequent exchange of energy between the electronic system and lattice through the electron phonon coupling results in rapid and localized heating. When the rate of heating sufficiently exceeds the rate of heat loss due to thermal conduction, lattice temperatures can exceed the melting point. Subsequent supercooling and quenching of molten zones is believed to be responsible for the observation of fully amorphous or partially amorphous regions along the particle trajectory. Contrary to many materials, which exhibit track melting and amorphization above a specific stopping power threshold, no experimental evidence of amorphization in SiC has been discovered [24].

An interesting relationship between the two stopping powers is observed in SiC. Irradiation with high velocity ions in the electronic energy loss regime is found to remove preexisting defects produced by lower energy ions in the nuclear energy loss regime [22] [25]. This suggests that the ion in the electronic regime imparts enough thermal energy to help anneal or recrystallize disordered SiC, but not enough to effectively amorphize the material. The reasons for this particular behavior are still a subject of investigation.

2.4. THE TWO TEMPERATURE MODEL

Ion tracks and the interaction of radiation with matter has been a subject of much research since the days of Thomson and Rutherford. Ion tracks are microstructural features that could be most generally described as regions of structurally modified

material that forms around the trajectory of an energetic ion. Several models have been proposed to explain the physics of ion track formation[26]. In the Coulomb explosion model, a charged particle that passes through a material ionizes and excites atoms, depleting a region of electrons and producing region of net positive charge ions. The resulting repulsive Coulomb force between ions leads to atomic displacement [27]. In the bond weakening model, the excitation and ionization produced by charged particle weaken the bonds between atoms which change the electron density around the atoms producing a force that can induce phase changes [28]. In the self-trapped exciton model a bound electron-hole pair produced via the excitation process may become self-trapped by lattice distortions. The resulting self-trapped exciton can decay radiatively or non-radiatively producing heat, transferring energy to impurities, and forming defects, exciton self-trapping is common in metal halides and rare-gas crystals[29].

Two Temperature Model (TTM) is a mathematical description of the inelastic thermal spike. The TTM was originally developed to describe the interaction of high power, pulsed laser radiation in solids. In the TTM, electrons and lattice constitute two subsystems, each at quasi-thermal equilibrium. That is to say, they each have a different but well-defined temperature. The electrons are initially excited by an external source, either a laser or swift charged particle. The actual interaction of the charged particle with electrons is a rather complex process but the TTM assumes that the electronic system rapidly thermalizes before any subsequent energy transport or transfer can occur.

The temperatures of the electrons and lattice evolve through a coupled pair of heat equations. The coupling is attributed to the electron-phonon interaction. The electron-phonon coupling factor acts as an energy channel between the two subsystems. Because

of the complexity of the electron-phonon interaction, it is usually treated as a fitting parameter, determined from measurements of track radius or is simply given an assumed value. The governing equations in the TTM are given by equations 2, and 3.

$$C_e \frac{\partial T_e}{\partial t} = \nabla \cdot [k_e \nabla T_e] - G\left(T_e - T_{ph}\right) + A(\boldsymbol{r}, t) \tag{2}$$

$$C_{ph} \frac{\partial T_{ph}}{\partial t} = \nabla \cdot \left[k_{ph} \nabla T_{ph}\right] + G(T_e - T_{ph}) \tag{3}$$

The subscripts ‘e’ and ‘ph’ denote thermal parameters for electrons and phonons (lattice). C_i is volumetric heat capacity, k_i is thermal conductivity, G is the electron-phonon coupling factor, and $A(\boldsymbol{r},t)$ is local and time-dependent electronic energy deposition term from the ion or laser. The heat capacities, and thermal conductivities of the electrons, and phonons are temperature dependent [30], [31], but in the case of the electron heat capacity and thermal conductivity, hot electrons in semiconductors and argued to behave like hot electrons in metals, and C_e is usually assumed to be around 1 J cm^{-3} K^{-1} and a k_e is treated as a constant.

2.5. ELECTRON-PHONON COUPLING

One of the most important quasi-particle interactions in solids is the electron-phonon interaction (EPI). Although it is usually ignored through the Born-Oppenheimer approximation, it is involved in several physical phenomena. It modifies the low energy excitations related to basic thermodynamic and mechanical properties [32], [33]. It is also related to basic transport properties such as the electrical and thermal conductivities. The lowest order electron-phonon interactions consist of Stoke and anti-Stokes processes where an electron absorbs or emits a phonon. The strength of the interaction vertex is

related to the strength of the deformation potential as felt by the incident and scattered electron wavefunctions when atoms are displaced along their normal mode coordinates.

The EPI also plays quite a prominent role in the BCS theory of superconductivity. Fifty years after the discovery of superconductivity, it was suggested that a weak interaction between electrons with opposite spin allows them to be coupled together as a bosonic *Cooper pair*, which then condense into a superconducting ground state. The potential was unknown until Fröhlich suggested that the electron-phonon interaction is responsible for Cooper pairing [34].

To develop a more exact description of the EPI, one should start with the Schrodinger equation for a system of nuclei and electrons.

$$\left(-\frac{\hbar}{2m}\sum_{i=1}^{N}\nabla_i^2-\frac{\hbar}{2M}\sum_{I=1}^{M}\nabla_I^2+\frac{1}{2}\sum_{i=1}^{N}\sum_{j\neq 1}^{N}\frac{e^2}{|\boldsymbol{r}_i-\boldsymbol{r}_j|}+\frac{1}{2}\sum_{I=1}^{M}\sum_{J\neq 1}^{M}\frac{Z_I Z_J e^2}{|\boldsymbol{R}_I-\boldsymbol{R}_J|}-\frac{1}{2}\sum_{I=1}^{M}\sum_{i=1}^{N}\frac{Z_I e^2}{|\boldsymbol{R}_I-\boldsymbol{r}_i|}\right)\Psi=E\Psi \tag{4}$$

The first term on the LHS is $\hat{T}_e$, the electron kinetic energy operator. Electrons have mass m and are indexed by i and j. The second term on the LHS is $\hat{T}_{ion}$, the ion kinetic energy operator. Here it is assumed all ions have the same mass and are indexed by I and J. The third term, $\hat{V}_{e-e}$, is the electron-electron potential energy operator. The fourth term is, $\hat{V}_{ion-ion}$, the ion-ion potential energy operator. The fifth term is $\hat{V}_{\boldsymbol{ion-e}}$, the ion-electron potential energy operator. r and R denote electron and nuclear coordinates, respectively. Ψ is the total wave function and E is the total energy. The EPI is embodied in the ion-electron potential energy operator.

Unfortunately, solutions of the all-electron Schrodinger equation are computationally costly for systems larger than a few atoms. Even if they were not, there is no guarantee that the solutions can be easily understood to the point of providing insight into the relevant physical process. Therefore, approximation methods are used to solve the Schrodinger equation. One of the most commonly used approaches is Density Functional Theory (DFT). DFT and related methods have proven to be useful tools in predicting material properties. In many cases they are able to provide accurate predictions of experimentally measurable values. More details about DFT will be discussed in the next section.

2.6. DENSITY FUNCTIONAL THEORY (DFT)

Description of the structure and dynamics of the many-electron system is a central problem in condensed matter physics and chemistry because it determines: the stability of matter, the chemical behavior of atoms, and transport properties. Some of these properties can be determined from the ground state [35]. Other properties require computation of excited states or use of perturbation theory. Exact analytical solutions to the Schrodinger equation (Eq. 4) with more than 1 electron (e.g. the helium atom) are not available. Thus, one must use approximate methods, numerical solutions, or a combination of the two.

Density Functional Theory (DFT) is a numerical approach that makes the large simplification of replacing the many-electron wavefunction with a one-electron wavefunction. The main advantages of DFT are computational efficiency (compared to all-electron methods), and enough accuracy to make quantitative predictions for a vast

number of material properties. For example, DFT and its extensions can be used to calculate band structure, optical absorption spectra, dielectric properties, formation enthalpies, elastic moduli, phase diagrams, and a host of other fundamental materials properties. Standard DFT methods usually treat nuclear coordinates as fixed values. However, DFT calculations of interatomic forces can be used to integrate the equations of motion for the nuclei in *ab-initio molecular dynamics*.

The main idea of DFT is to replace the many-body wavefunction with an electron density, i.e. convert the 3N variable problem to a 3 variable problem. The electron density is solved in a self-consistent manner by minimizing a functional (function of a function) which describes the kinetic, potential, exchange, and correlation energies of the system. To give an idea of computational advantages of DFT, the computational cost (number of operations) of all-electron methods such as the Hartree-Fock method formally scale as $O(N^4)$ where N is the number of electrons in the system. DFT methods which rely on matrix diagonalization scale as $O(N^3)$ though some methods scale as O(N). While such a difference may not be significant for, say, modeling a H_2 molecule, a system with, say, 100 carbon atoms (600 electrons) will quickly become daunting.

While DFT is successful at predicting many physical properties, it essentially treats the problem of electronic structure determination as a problem consisting of one-electron in an effective potential. This means that phenomena involving multiple electrons are not always well modeled by DFT. Some examples include calculations of dispersion forces which include many-body correlations, strongly correlated systems where electron-electron interactions at the same site make a significant contribution to the

total energy, and calculations of the band gap where both one particle and two particle excitations contribute.

2.7. DEVELOPMENT OF DFT

In the Born Oppenheimer or adiabatic approximation, one assumes that the ions or nuclei are much heavier and slower than electrons and can be regarded as stationary. This is justified on the grounds that nucleons are over 1800 times more massive than electrons. With the Born-Oppenheimer approximation in place, the Schrodinger equation becomes

$$\left(-\frac{\hbar}{2m}\sum_{\boldsymbol{i=1}}^{\boldsymbol{N}}\nabla_i^2+\frac{1}{2}\sum_{\boldsymbol{i=1}}^{\boldsymbol{N}}\sum_{\boldsymbol{j\neq 1}}^{\boldsymbol{N}}\frac{e^2}{|\boldsymbol{r_i}-\boldsymbol{r_j}|}+\frac{1}{2}\sum_{\boldsymbol{I=1}}^{\boldsymbol{M}}\sum_{\boldsymbol{i=1}}^{\boldsymbol{N}}\frac{Z_I e^2}{|\boldsymbol{R_I}-\boldsymbol{r_i}|}\right)\Psi = E\Psi \tag{5}$$

We denote the total wave function that describes the many-particle system as $\Psi(\boldsymbol{r_1}, \boldsymbol{r_2}, \ldots, \boldsymbol{r_N})$. For simplicity, the spin indices of the electrons will be dropped. The marginal probability of measuring electron 1 at $\boldsymbol{r_1}$ is

$$\rho(\boldsymbol{r_1}) = \int d\boldsymbol{r_2} \ldots d\boldsymbol{r_N}|\Psi(\boldsymbol{r_1}, \boldsymbol{r_2}, \ldots, \boldsymbol{r_N})|^2 \tag{6}$$

The Hartree approximation represents the total wave function as a product of one-electron wave functions[36], i.e. $\Psi = \psi_1(r_1)\psi_2(r_2)\psi_3(r_3)..\psi_N(r_N)$. If we do not care about the identity of the electron measured at a particular coordinate, the electron density, under the Hartree approximation, reduces to a simple sum of marginal probabilities.

$$n(\boldsymbol{r}) = 2\sum_i \psi_i^*(r)\,\psi_i(r) \tag{7}$$

2 accounts for spin. $\psi_i^*(r)$ is the complex conjugate of $\psi_i(r)$. Equation 6 implies that the one-electron wave functions provide the electron density. In fact, the ground state density also contains all information about the ground state wave function. Thus, a system of N particles with 3N variables can be transformed into a problem of 3 variables.

Hohenberg and Kohn proved two theorems, the Hohenberg-Kohn (HK) theorems. The first is that energy is a functional of density, $E[n(r)]$. This follows from the fact that density is a composite function of wave function. The second HK theorem states that the density that minimizes the energy is the electron density corresponding to the ground state solution of the time-independent Schrödinger equation[37].

The energy functional can be divided into two parts, an exactly known part and an unknown exchange part

$$E[(\psi_i)] = E_{known}[(\psi_i)] + E_{xc}[(\psi_i)] \tag{8}$$

The exactly known part is

$$E_{known}[\{\psi_i\}] = -\frac{\hbar}{m}\sum_i \int \psi_i{}^* \nabla^2 \psi_i d\boldsymbol{r}^3 + \int V(\boldsymbol{r}) n(\boldsymbol{r}) d\boldsymbol{r}^3 + \frac{e^2}{2}\int\int \frac{n(\boldsymbol{r}) n(\boldsymbol{r}')}{|\boldsymbol{r}-\boldsymbol{r}'|} d\boldsymbol{r}^3 d\boldsymbol{r}'^3 + E_{ion} \tag{9}$$

This contains the kinetic energy term, potential energy of electrons interacting with the nuclear/ionic potential, and the electron-electron Coulomb interaction.

The exchange part includes effects not incorporated in the known part, exchange and correlation effects. Kohn and Sham showed that the electron density can be expressed as a solution to a set of one-particle equations (Khon-Sham equations).

$$\left[\frac{-\hbar^2}{2m}\nabla^2 + V(\boldsymbol{r}) + V_H(\boldsymbol{r}) + V_{XC}(\boldsymbol{r})\right]\psi_{\boldsymbol{i}}(\boldsymbol{r}) = \varepsilon_i\psi_i \quad (10)$$

$V_H(\boldsymbol{r}) = e^2\int\frac{n(\boldsymbol{r'})}{|\boldsymbol{r}-\boldsymbol{r'}|}d^3\boldsymbol{r'}$ is called the Hartree potential, and $V_{XC}(r) = \frac{\delta E_{XC}(\boldsymbol{r})}{\delta n(\boldsymbol{r})}$ is the exchange potential. To solve the Kohn-Sham equations, $V_H(\boldsymbol{r})$ is required. To determine the Hartree potential a density is required. To determine the density, the electron wave functions are required which requires solving the Kohn-Sham equations. Because of the circularity of the problem, the problem must be solved in a self-consistent way where an initial guess updated iteratively. The process continues until the solution converges. In practice, a convergence criterion is imposed based on the accuracy needs. The process is illustrated in Figure 2.6. Ultimately, the wavefunction, density, and Hartree potential are simultaneously obtained.

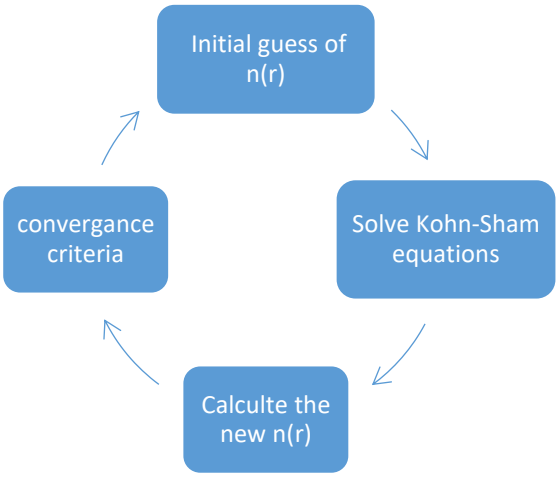

Figure 2.6. Self-Consistent Field (SCF) calculations to solve DFT Kohn-Sham equations

The main technical difficulty that arises is the choice of the exchange correlation functional. As the exact functional is not known, a suitable assumption must be used. Different approximations for exchange-correlation can be used. One of the simplest and most widely used is Local Density Approximation (LDA). The LDA assumes that the functional only depends on the product of the electron density and an energy function (not functional) which depends only on the local magnitude of the density.

$$E_{XC} = \int \epsilon_{XC}(n(\boldsymbol{r}))n(\boldsymbol{r})d\boldsymbol{r} \tag{11}$$

Because the energy function only depends on the local electron density, calculations of the homogeneous electron gas can be employed. In the homogeneous electron gas (or Jellium) model, electrons are placed in a uniform positive background charge. ϵ_{XC} can be divided into two parts, ϵ_X and ϵ_C, the exchange part and correlation part, respectively. The exchange part is determined using the Slater-Dirac model. The correlation part can be parameterized by quantum Monte Carlo simulations of the homogenous electron gas.

An improved approximation to the exchange-correlation functional is the Generalized Gradient Approximation (GGA). In the GGA, the functional depends not only on the local density but also on the gradient of the density. Meta-GGA incorporates the Laplacian of the density. Other exchange-correlation approximations exist but increasing accuracy demands more calculation time and computing power. Figure 2.7 illustrates some of these approximations and ranks them according to accuracy. This is the so-called Jacob's ladder of DFT accuracy.

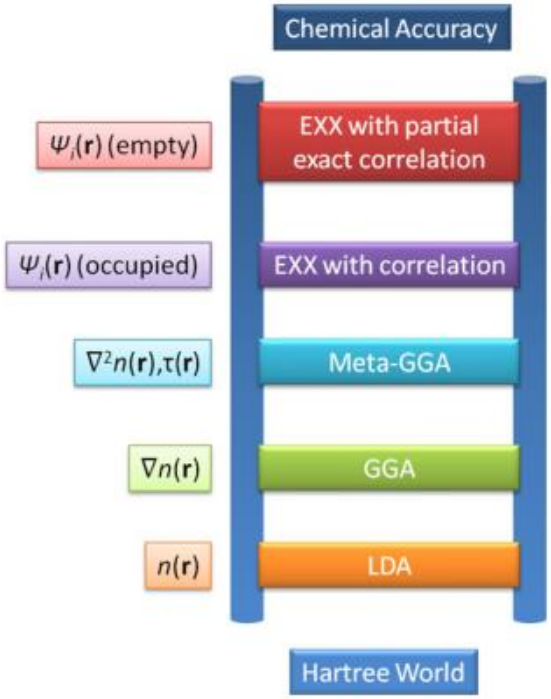

Figure 2.7: Jacob's ladder of approximation accuracy[38]

2.8. DENSITY FUNCTIONAL PERTURBATION THEORY

2.8.1. Lattice Vibrations. The description of lattice vibrations (phonons) is important in the discussion of properties such as lattice specific heat, heat conduction, the electron-phonon interaction, and electrical conductivity. The basic problem of studying lattice vibrations is solving for the frequencies and polarization vectors (eigen displacements) for the lattice normal modes. The Born-Oppenheimer approximation allows one to consider the nuclear Hamiltonian separately.

$$H = -\sum_I \frac{\hbar^2}{2M_I}\frac{\partial^2}{\partial \boldsymbol{R}_I^2} + E(\{\boldsymbol{R}\}) \tag{12}$$

M_I and $\boldsymbol{R}_I$ are the mass and the coordinate of the I[th] ion. $E(\{\boldsymbol{R}\})$ is the ground state energy of a Hamiltonian, H_R, of N interacting electrons moving in a field of fixed nuclei at coordinates **R**.

$$H_R = -\frac{\hbar}{2m}\sum_i \frac{\partial^2}{\partial \boldsymbol{r}_i^2} + \frac{e^2}{2}\sum_{i\neq j}\frac{1}{|\boldsymbol{r}_i - \boldsymbol{r}_j|} + \sum_{i,I} \upsilon_I(\boldsymbol{r}_i - \boldsymbol{R}_I) + E_N(\{\boldsymbol{R}\}) \tag{13}$$

As before, $\boldsymbol{r}_i$ are the electron coordinate, and *m* and *e* are electron mass and charge. $\upsilon_I = -\frac{Z_I e^2}{r}$ is the electron-nucleus Coulomb interaction, and

$$\boldsymbol{E_N} = \frac{e^2}{2}\sum_{\boldsymbol{I\neq J}}\frac{Z_I Z_J}{|\boldsymbol{R_I} - \boldsymbol{R_J}|} \tag{14}$$

is the nuclear electrostatic energy. Z_J is the nuclear charge. Forces on nuclei, $\boldsymbol{F}_I$, are given by the Hellmann–Feynman theorem which leads to

$$\boldsymbol{F}_I = -\frac{\partial E(\{\boldsymbol{R}\})}{\partial \boldsymbol{R}_I} = -\left\langle \Psi_{\{\boldsymbol{R}\}} \middle| \frac{\partial H_{\{\boldsymbol{R}\}}}{\partial \boldsymbol{R}_I} \middle| \Psi_{\{\boldsymbol{R}\}} \right\rangle \tag{15}$$

$\Psi_{\{\boldsymbol{R}\}}$ is the ground state electronic wave function for a given set of nuclear coordinates. Thus, the results of the self-consistent Kohn-Sham calculation can be inserted into equation 15 to determine interatomic forces.

Once the interatomic forces are known, calculation of the eigenfrequencies, ω, and polarization vectors (eigen displacements) are obtained by solving the secular equation

$$\sum_{J,\beta}\left(C_{IJ}^{\alpha\beta} - M_I\omega^2\delta_{IJ}\delta_{\alpha\beta}\right)U_J^{\beta} = 0 \tag{16}$$

U_I^α is the eigendisplacement of the I_{th} atom along coordinate α. $C_{IJ}^{\alpha\beta}$ is the interatomic force constant matrix (IFC matrix). The IFC matrix is given by

$$C_{IJ}^{\alpha\beta} = \frac{\partial^2 E(\{R\})}{\partial R_I^\alpha \partial R_J^\beta} = -\frac{\partial F_I^\alpha}{\partial R_J^\beta} \tag{17}$$

Empirical or semiempirical interatomic potentials can be used to calculate IFCs. In general, the parameters of these models come from fitting experimental data, such as sound speeds, IR and Raman spectra, and inelastic neutron scattering spectra. However, DFT provides a mean of calculating the IFCs from first principles.

2.8.2. Perturbation Theory Calculation of the electron-phonon coupling relies on perturbation theory. In perturbation theory we start with an unperturbed Hamiltonian and solve the eigenvalue equation.

$$H^0|\Psi_i^0\rangle = \varepsilon_i^0|\Psi_i^0\rangle \tag{18}$$

The unperturbed wavefunction and its eigenenergy is usual describes a simple situation such as a freely propagating non-interacting particle. In the case of the electron-phonon interaction, $|\Psi_i^0\rangle$ will be identified as a Bloch wave.

The Hamiltonian is modified by gradually turning perturbation terms through a continuous variable λ

$$H^0 \to H^0 + \lambda H^1 + \lambda^2 H^2 + \cdots$$

This will result in shifts in the eigen energies as well as perturbations to the wavefunctions. Derivations can be found in many standard quantum mechanics textbooks [39][40]. Suffice to say, the first energy correction is given by

$$\varepsilon_i^1 = \langle\psi_i^0|H^1|\psi_i^0\rangle \tag{19}$$

while the first order correction to the wavefunction is

$$\left|\psi_i^1\right\rangle = \sum_j \left|\psi_i^0\right\rangle \frac{1}{\varepsilon_i^0 - \varepsilon_j^0} \left\langle\psi_j^0\right|H^1\left|\psi_i^0\right\rangle \tag{20}$$

In the context of the electron-phonon coupling, the first order perturbation to the Hamiltonian, H^1, will be due to small displacements of atoms along normal modes. The term $\left\langle\psi_j^0\right|H^1\left|\psi_i^0\right\rangle$ will eventually be identified as the electron-phonon matrix element.

2.9. ELECTRON SELF-ENERGY

The electron self-energy has been a problem since the development of classical electromagnetism. In classical electromagnetism the self-energy represents the interaction of an electron with its own electric field. One can show that the field energy, $E_e = e^2/r_e$, goes to infinity as the electron radius, r_e, goes to zero. Cutting this self-energy at the electrons rest mass defines a classical electron radius. In quantum theory the problem is made more difficult because electrons are assumed to be point particles. The electron also possesses intrinsic spin which adds a magnetic field contribution to the self-energy.

The simplest definition of the electron self-energy in the many-body problem is the difference between quasiparticle energy associated particle interacting with its surroundings and the energy of the bare particle. The electron gains (or loses) energy and mass through its interactions with the lattice potential, phonons, electrons, and other quasi-particles[41]. If one only considers interactions between electrons and phonons the electron gains self-energy through processes such as those seen in Figure 2.8.

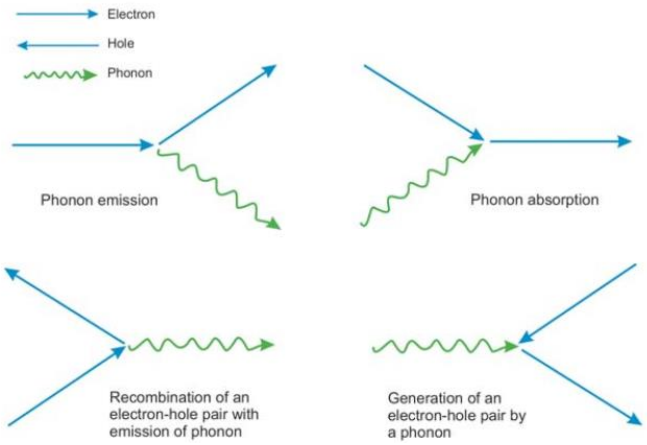

Figure 2.8: Illustration of some possible electron phonon interactions[34]

In order to calculate the electron-phonon coupling factor, it will be necessary to calculate the electron scattering rate. This scattering rate is related to the imaginary part of the electron self-energy. The mode resolved scattering rate (inverse of relaxation time), can be calculated using the imaginary part of the self-energy, $\sum_{\boldsymbol{nk}}$ [33][42]

$$\begin{aligned}\frac{1}{\tau_{\boldsymbol{nk}}} &= 2\mathrm{Im}\sum_{\boldsymbol{nk}} \\ &= \frac{2\pi}{\hbar}\sum_{m\nu}\int \frac{d\boldsymbol{q}}{\Omega_{BZ}}|g^{\nu}_{mn}(\boldsymbol{k},\boldsymbol{q})|^2\left[\left(1-f_{\boldsymbol{mk+q}}+\ n_{\boldsymbol{q}\nu}\right)\delta\left(\varepsilon_{n\boldsymbol{k}}\right.\right. \\ &\qquad \left.-\varepsilon_{\boldsymbol{mk+q}}-\hbar\omega_{\boldsymbol{q}\nu}\right) \\ &\qquad \left.+\left(f_{\boldsymbol{mk+q}}+\ n_{\boldsymbol{q}\nu}\right)\delta\left(\varepsilon_{nk}-\varepsilon_{\boldsymbol{mk+q}}+\hbar\omega_{\boldsymbol{q}\nu}\right)\right]\end{aligned} \tag{21}$$

n and $\boldsymbol{k}$ are the branch and wavevectors for the electron undergoing scattering. $g^{\nu}_{mn}(\boldsymbol{k},\boldsymbol{q})$ are the electron-phonon matrix elements which are equal to $\langle\psi_{\boldsymbol{mk+q}}|\partial_{\boldsymbol{q}\nu}V|\psi_{n\boldsymbol{k}}\rangle$. The matrix elements represent the amplitude for an electron with wavevector $\boldsymbol{k}$ in band n to scatter into wavevector $\boldsymbol{k}+\boldsymbol{q}$ in band m. $\partial_{\boldsymbol{q}\nu}V$ is the derivative of the effective potential felt by electrons with respect to atomic displacements for a phonon with wavevector $\boldsymbol{q}$ on

branch ν. Ω_{BZ} is the Brillouin zone volume, $f_{m\boldsymbol{k+q}}$ are the Fermi occupation numbers for electrons, $n_{\boldsymbol{q}\nu}$ are the Bose occupation numbers for phonons. It is here assumed that the electron and phonon occupation numbers are calculated at different temperatures. ε_{nk} and $\hbar\omega_{q\boldsymbol{\nu}}$ are electron and phonon energies.

2.10. EPC IN METALS

Much research has been conducted on the EPC in metals. In metals at near 0 K, an EPC *constant* can be defined. Essentially, the small magnitude of phonon energies ensures that electrons can only scatter from states near the Fermi surface to states near the Fermi surface. In semiconductors and insulators, where there is no Fermi surface, the EPC is not embodied in a single constant. DFT calculations of the EPC constant have been performed for various metals and alloys and have been experimentally validated using tunneling experiments. The influence of each phonon branch has been studied. The EPC strongly depends on the phonon density of states and the electronic structure. In free-electron-like aluminum, longitudinal phonons make a significant contribution to the EPC, while the acoustic transverse (AT) and acoustic longitudinal (AL) branches are found to dominate the contribution in copper alloys like $CuAu_3$. In noble metals, transverse phonons dominate the EPC [43]. Figure 2.9 show results of EPC of some metals and alloys. One of the key features of the EPC in metals is the comparatively weak temperature dependence, varying, perhaps by less than two orders of magnitude over several thousand degrees. This weak dependence will be relevant later in Chapter 3, where insulators and metals are compared.

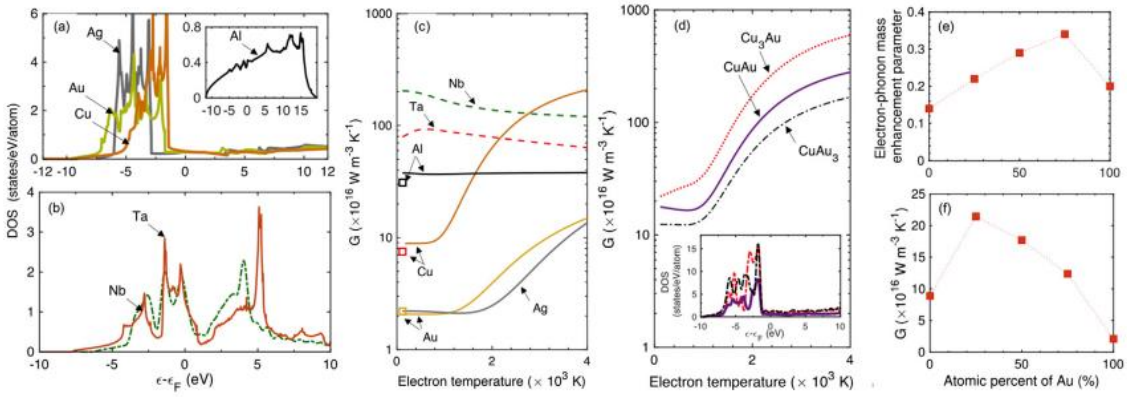

Figure 2.9: Electronic density and EPC in some metals (a) The electronic density of states of Au, Cu, Ag, Al, (b) The electronic density of states of Ta, and Nb, (c) The electron-phonon coupling constant for some metals as a function of electronic temperature, (d) The electron-phonon coupling constant for some Cu alloys as a function of electronic temperature, (d) Electron-phonon coupling strength for the copper-gold alloys as a function of atomic percentage of gold. (f) G as a function of atomic percentage of gold for the copper-gold alloys[43]

In metals, it is popular to use the rigid muffin tin approximation to calculate the EPC constant. The potential derivative, $\boldsymbol{\delta V}$, is replaced by the gradient of the Muffin-tin potential which would enter an augmented plane wave band calculation [44]. With such an approach, the electron-phonon matrix elements are easily obtained. Predictions with this method have agreed with experimental results, but cannot be extended to a defective lattice.

Other computational studies have worked within the tight-binding approximation. This semi-empirical method is used to calculate the band structure of single-particle Bloch states written as linear combinations of atomic orbitals[45]. This approximation offers the possibility of estimating the EPC in a wide range of simple metals. Medvedev et al. [46] studied several simple metals, and different structures using the tight-binding approximation. The best agreement with experiments and other numerical methods was

found at higher electronic temperatures where the electrons better resemble free electrons.

Fully ab-initio calculation is also possible for pure materials. DFT and perturbation theory is the most common and accurate approach to calculating the EPC. The main disadvantage of DFT calculations is the computational cost. Zhibin *et al*. used fully ab-initio calculated electron density of states (DOS) to calculate electron-phonon coupling constant (G), and electronic heat capacity (C_e) for eight representative metals: Al, Cu, Ag, Au, Ni, Pt, W, and Ti, [47]. They investigated the relationship between the coupling and temperature through ultrafast laser pulse irradiation using the Two Temperature Model (TTM). That investigation revealed that the DOS is sensitive to thermal excitation and can lead to a large variation of thermophysical properties in the case of electron-phonon nonequilibrium. This latter point suggests that the electron phonon coupling in semiconductors and insulators may be even more sensitive to thermal excitation. It is known, for example, that electrical conductivity in semiconductors is strongly affected by thermal carrier generation. Furthermore, the EPC constant calculated at cryogenic temperature assumes that the Fermi surface is thin, all scattering occurs within a narrow range within the DOS. At the high temperatures produced by a swift heavy ions, electrons and holes are not necessarily guaranteed to lie close the conduction band minimum or valence band maximum. All of these factors suggest that a different approach must be tried in order to address the problem of the electron phonon coupling in SiC.

PAPER

I.VACANCY-INDUCED ENHANCED OF ELECTRON-PHONON COUPLING IN CUBIC SILICON CARBIDE AND ITS RELATIONSHIP TO TWO TEMPERATURE MODEL

Salah Al Smairat, Joseph Graham

Department of Nuclear Engineering and Radiation Science
Missouri University of Science and Technology, Rolla, MO 65409

ABSTRACT

The electron-phonon coupling factor was calculated for both pristine and vacancy-rich 3C-SiC. *Ab initio* calculations were performed within the framework of density functional perturbation theory. Wannier functions were used to interpolate eigenvalues into denser grids through the Electron-Phonon using Wannier (EPW) code. The coupling factor was determined through calculations of the electron self-energy, electron-phonon relaxation time, and electronic specific heat. These parameters were extrapolated to high temperatures using a hybrid model which mixes band calculations for electrons below an energy cutoff with the free electron gas model for electrons above the energy cutoff. The electron relaxation times, specific heats, electron drift mobilities, and electron-phonon coupling factors were calculated as a function of electron temperature. Si and C vacancies were found to have a profound effect on electron-phonon coupling for all temperatures, while electronic specific heat capacity was found to be most affected at cryogenic temperatures. The electron drift mobility was calculated at

different temperatures using the scattering time. Calculated mobilities were validated with Hall mobility measurements reported in the literature. The importance of structural defects on the electron-phonon coupling is discussed in the context of the two-temperature model, a model which has been widely used to understand aspects of the interaction of solids with pulsed laser irradiation and swift heavy ion irradiation.

*Corresponding Author: grahamjose@mst.edu

1. INTRODUCTION

Silicon carbide is a high-temperature ceramic with numerous commercial and industrial uses. Its utility arises from a combination of desirable properties such as high hardness, high thermal conductivity, low coefficient of thermal expansion, semiconducting properties, and radiation tolerance [1,2]. In the nuclear power industry, SiC is used in High-Temperature Gas-Cooled Reactors as a coating in Tri-Isostructural (TRISO) fuel particles. It is also being considered as a cladding material in light water reactors [1, 3] and as a structural material in the flow channels of fusion systems [49].

Materials in nuclear energy systems are exposed to intense fields of neutrons, gamma rays, and fission products. The interaction of radiation with matter results in the transfer of energy from incident particle to the lattice through nuclear energy loss and to electrons through electronic energy loss [50]. The former can produce structural disorder through the introduction of elementary point defects such as vacancies and self-interstitials. Higher-order defects such as clusters, dislocations, and voids can subsequently form and grow [51]. Electronic energy loss describes the excitation of the

electronic structure and generation of delta electrons. Energy transfer from the electronic system to the lattice is mediated, to a large extent, by electron-phonon coupling [7], though in semiconductors, trap-assisted radiative and non-radiative recombination processes are also important [8]. Understanding electron-phonon coupling in the presence of structural defects and as a function of electron temperature is an important element in developing a complete picture of radiation interactions and radiation effects when both nuclear and electronic energy loss mechanisms are present. In SiC, an interesting competitive relationship between nuclear and electronic energy loss was recently observed [9]. Structural disorder produced in SiC with ions in the nuclear energy loss regime was found to be partially annealed upon irradiation with ions in the electronic energy loss regime. Reasons for this may stem from modulation of the electron-phonon coupling and thermal diffusivity via defects. This manuscript examines the former.

The electron-phonon interaction is also an important quasi-particle interaction that modifies both the electron and phonon self-energies in a material. It is, therefore, connected to the basic thermodynamic and transport properties of the material [10]. The electron-phonon coupling factor discussed in this work is the dimensionful factor appearing in the two-temperature model, a model which has been used to describe the transfer of energy from hot electrons to a lattice [11,12]. The two-temperature model is expressed through the following equations:

$$C_e \frac{\partial T_e}{\partial t} = \nabla \cdot [k_e \nabla T_e] - G\left(T_e - T_{ph}\right) + A(\boldsymbol{r}, t) \quad (1)$$

$$C_{ph} \frac{\partial T_{ph}}{\partial t} = \nabla \cdot \left[k_{ph} \nabla T_{ph}\right] + G(T_e - T_{ph}) \quad (2)$$

$A(\boldsymbol{r}, t)$ represents the space- and time-dependent energy source (e.g. pulsed laser or swift charged particle). C_e and C_{ph} are the specific heat capacities of electrons and the lattice, respectively. k_e and k_{ph} are the corresponding thermal conductivities for electrons and the lattice. T_e and T_{ph} are the temperatures of the electrons and the lattice, respectively. In the two-temperature model, it is assumed that electrons and the lattice are at quasi-thermodynamic equilibrium, which is to say that energy is rapidly shared among electrons establishing a well-defined local electron temperature, and energy is efficiently shared among phonons establishing a well-defined local lattice temperature. The two temperatures can be different owing to the slow transfer of energy from electrons to lattice. The rate of energy transfer is governed by $G(T_e - T_{ph})$.

Various approaches for determining G have been made. Here we follow the approach of [13] which takes as the value of G

$$G = \frac{C_e}{\tau} \tag{3}$$

τ is the electron-phonon relaxation time (inverse scattering rate). It should be mentioned that the *dimensionless* electron-phonon coupling constant - which frequently appears in the context of superconductivity in metals - can also be related to the dimensionful factor [14, 15]. Though well-defined for metals at cryogenic temperatures, the dimensionless constant presupposes that only electron scattering at the Fermi surface contributes to energy transfer [52]. In bandgap materials, electron-phonon scattering occurs in the conduction and valence bands. Therefore, the factor discussed from this point forth pertains only to the definition in Eq. 3.

The main goal of this study is to understand the effect of Si and C vacancies on electron-phonon coupling in cubic SiC. Using density functional perturbation theory, the electron-phonon coupling factors and conduction electron lifetimes were calculated in pristine 3C-SiC and in relaxed supercells of 3C-SiC containing Si or C vacancies. The model was validated through comparison of predicted electron drift mobilities and electron Hall mobility measurements, reported in the literature.

2. THEORY AND METHODOLOGY

2.1. THE ELECTRON RELAXATION TIME

The electron relaxation time is related to the imaginary part of the electron self-energy, $\sum_{n\boldsymbol{k}}$ (with band n and wavevector $\boldsymbol{k}$). In the Migdal approximation, the mode-resolved scattering rates (inverse relaxation times) are given by [16].

$$\frac{1}{\tau_{n\boldsymbol{k}}} = 2\mathrm{Im}\sum_{n\boldsymbol{k}} \tag{4}$$

$$= \frac{2\pi}{\hbar}\sum_{m\nu}\int \frac{d\boldsymbol{q}}{\Omega_{BZ}} |g^{\nu}_{mn}(\boldsymbol{k},\boldsymbol{q})|^2 \big[\big(1 - f_{m\boldsymbol{k}+\boldsymbol{q}} + n_{\boldsymbol{q}\nu}\big)\delta\big(\varepsilon_{n\boldsymbol{k}} - \varepsilon_{n\boldsymbol{k}+\boldsymbol{q}} - \hbar\omega_{\boldsymbol{q}\nu}\big)$$

$$+ \big(f_{m\boldsymbol{k}+\boldsymbol{q}} + n_{\boldsymbol{q}\nu}\big)\delta\big(\varepsilon_{nk} - \varepsilon_{n\boldsymbol{k}+\boldsymbol{q}} + \hbar\omega_{\boldsymbol{q}\nu}\big)\big]$$

where $g^{\nu}_{mn}(\boldsymbol{k},\boldsymbol{q})$ are the electron-phonon matrix elements:

$$g^{\nu}_{mn}(\boldsymbol{k},\boldsymbol{q}) = \langle \psi_{m\boldsymbol{k}+\boldsymbol{q}} | \partial_{\boldsymbol{q}\nu} V | \psi_{n\boldsymbol{k}} \rangle \tag{5}$$

$\partial_{\boldsymbol{q}\nu} V$ is the partial derivative of the effective potential with respect to the lattice normal mode indexed by wave vector $\boldsymbol{q}$ and branch ν. Each electron-phonon matrix element represents the transition amplitude for an electron in state $\psi_{n\boldsymbol{k}}$ (with wave vector $\boldsymbol{k}$ and

branch n) to scatter into state $\psi_{m\boldsymbol{k+q}}$ due to the perturbation in the effective potential resulting from atomic motion. $f_{m\boldsymbol{k+q}}$ are the Fermi occupation numbers for electrons and $n_{\boldsymbol{q}\nu}$ are the Bose occupation numbers for phonons. It is here assumed that the electron and phonon occupation numbers are calculated at different temperatures. $\varepsilon_{n\boldsymbol{k}}$ and $\hbar\omega_{\boldsymbol{q}\nu}$ are electron and phonon energies, respectively. The integral is performed over the first Brillouin zone, which has volume Ω_{BZ}.

2.2. CALCULATIONS OF MATRIX ELEMENTS

Density functional perturbation theory (DFPT) calculations were performed on 2×2×2 supercells of 3C-SiC. After relaxing the atomic coordinates to minimize total energy, ground state wave functions were calculated on a uniform 6×6×6 k-grid with a cut-off energy of 60 Ry using the Quantum Espresso code [17]. Phonon frequencies and polarization vectors were calculated on a uniform 3×3×3 q-grid centered at Γ using the perturbation theory method. The resulting polarization vectors were used to deform the effective potential along phonon normal coordinates, taking $V \rightarrow V + \partial_{\boldsymbol{q}\nu} V$. The matrix elements were then determined by taking the product of the in and out Bloch states with the perturbing potential (Eq. 5).

The resulting matrix elements were Wannierized and interpolated onto a 12×12×12 k-grid, and 46×46×46 q-grid using the Electron-Phonon using Wannier (EPW) code [18],[19]. The density of the k-point grid was increased until the maximum differences in the imaginary electron self-energy converged to within 5%. This resulted in a final interpolated grid of 12×12×12 for the k-point grid and 46×46×46 for the q-point grid. EPW was subsequently used to determine the electron self-energies and relaxation

times. Calculations in defective supercells of SiC were performed by adding a single C or Si vacancy into the supercell and relaxing the structure. This corresponded to C or Si vacancy concentrations of 12.5%. Those defective supercells will hereafter be referred to as $SiC_{0.875}$ or $Si_{0.875}C$. Initial projections used sp^3 hybridized orbitals for the pristine cell and random projections for the defective cells.

Relaxation times were calculated from 20 K to 10^6 K. In order to parameterize the relaxation time as a function of electron temperature, several simplifying assumptions were made. The electron temperature dependence appears through the Fermi occupation numbers in Eq. 4. The use of Fermi-Dirac statistics for the electron system assumes that the hot electrons and holes have established quasi-thermal equilibrium, which is to say that they can be characterized by a single electron temperature. In the context of the two-temperature model, where a rapid excitation source is present, such an assumption is likely only valid after an initial equilibration period has elapsed and provided that the electron-electron interaction rate is significantly greater that the electron-phonon scattering rate. Alternative approaches might also consider using quasi-Fermi levels for both electrons and holes or using Boltzmann transport or Monte Carlo methods to study the non-equilibrium dynamics. However, in the context of the two-temperature model, it is necessary to parameterize all material properties by a single electron temperature and single lattice temperature.

2.3. HYBRID MODEL OF SPECIFIC CAPACITY AND THE ELECTRON-PHONON COUPLING FACTOR

At low and intermediate temperatures, the Fermi occupation numbers are negligibly small above the highest band energies, E_{max}, calculated using the DFT code

(approx. 11 eV above the Fermi level). However, above about 10^5 K, the number of electrons above the highest energy bands begins to become non-negligible. The contribution of those high energy electrons is approximated by treating them as a free electron gas obeying Boltzmann statistics. The use of Boltzmann statistics is justified as high energy states are sparsely occupied. The hybrid electronic specific heat capacity is therefore made up of two parts:

$$C_e(T) = \frac{2}{N_k}\sum_{n\boldsymbol{k}} C_{n\boldsymbol{k}} + \frac{3}{2}k_B n_{free}(T) \tag{6}$$

The first term is the heat capacity determined from the static band calculations. The second term is the specific heat capacity of a Maxwell-Boltzmann distributed gas of free electrons and is only important above 10^5 K. $C_{n\boldsymbol{k}}$ are the mode-resolved electronic heat capacities due to electrons in the calculated band structure, which has a maximum energy of E_{max}.

$$C_{n\boldsymbol{k}} = \frac{\left(\epsilon_{n\boldsymbol{k}} - \epsilon_f\right)^2 \exp\left(\frac{\epsilon_{n\boldsymbol{k}} - \epsilon_f}{k_B T}\right)}{k_B T^2 \left[1 + \exp\left(\frac{\epsilon_{n\boldsymbol{k}} - \epsilon_f}{k_B T}\right)\right]^2} \tag{7}$$

ϵ_f is the Fermi level and N_k is the number of sampled wavevectors in the Brillouin zone (N_k=1728 for these calculations). The factor of 2 appearing before the first term in Eq. 6 accounts for electron spin.

To connect Fermi-Dirac statistics for electrons below E_{max} with Boltzmann statistics above E_{max}, the following approximation is used for the product of the electronic density of states D, and the Fermi-Dirac distribution f.

$$D(\epsilon)f\left(\epsilon-\epsilon_f;T\right)\cong\exp\left(-\frac{E_{max}-\epsilon_f}{k_BT}\right)\exp\left(-\frac{\epsilon-E_{max}}{k_BT}\right)D_{MB}(\epsilon-E_{max}) \quad (8)$$

where $\epsilon > E_{max}$ and D_{MB} is the density of states of a Maxwell-Boltzmann gas. Integrating Eq. 8 over energy gives the number of free electrons:

$$n_{free}(T)=\int_{E_{max}}^{\infty}D(\epsilon)f\left(\epsilon-\epsilon_f;T\right)d\epsilon=N\exp\left(-\frac{E_{max}-\epsilon_f}{k_BT}\right) \quad (9)$$

N is the total number of valance electrons of SiC. For high temperatures, the Fermi level was adjusted to ensure the conservation of valence electrons. At temperatures below 10^4 K, no adjustment of the Fermi level was needed. While such a treatment of the high-energy electrons is highly approximate, it is necessary to account for their energy contributions in some way. Otherwise, the specific heat capacity will be unphysically low at high temperatures and may even decrease. Note that in this scheme, each valence electron in the structure has one valence state, one conduction/excited state, and one free particle state. Extending Eq. 3 and incorporating the contribution of free electrons to the electron-phonon coupling factor, one obtains:

$$G=\frac{2}{N_k}\sum_{n\boldsymbol{k}}\frac{C_{n\boldsymbol{k}}}{\tau_{n\boldsymbol{k}}}+\frac{3k_Bn_{free}(T)}{2\tau_{free}(T)} \quad (10)$$

The relaxation time for free electrons, $\tau_{free}(T)$, is approximated as follows. The scattering rate is given by.

$$\frac{1}{\tau_{free}(T)}=\bar{\Sigma}\langle v\rangle \quad (11)$$

where the mean cross-section, $\bar{\Sigma}$, is assumed to be a sum of geometric cross sections for ionic cores.

$$\bar{\Sigma} = \rho_C \sigma_C + \rho_{Si} \sigma_{Si} = \rho_C (\pi r_c^2) + \rho_{Si} (\pi r_{Si}^2) \tag{12}$$

ρ_C and ρ_{Si} are the number densities of carbon and silicon atoms. r_C and r_{Si} are the ionic radii. The mean velocity of the free electrons, $\langle v \rangle$, which is also the mean velocity of a Maxwell-Boltzmann gas is:

$$\langle v \rangle = \sqrt{\frac{8 k_B T}{\pi m_e}} \tag{13}$$

where m_e is the electron mass.

2.4. ELECTRON MOBILITIES AND THE ELECTRON-PHONON MEAN FREE PATH

In order to validate these first principles calculations with experimental data, the electron drift mobilities were calculated and compared to experimentally measured electron Hall mobilities in donor doped 3C-SiC. The electron drift mobility can be obtained from the conduction electron relaxation time using:

$$\mu_e = \frac{e\tau}{m_e^*} \tag{14}$$

where τ is the thermal-averaged conduction electron relaxation time and m_e^* is the effective mass of the electrons. μ_e is measured by applying a magnetic field perpendicular to the carrier currents that are induced by an electromotive force. This in turn produces a potential difference, the Hall voltage V_H [20], which can be measured and

used to extract the Hall mobilities for electrons and holes. The electron mobility was calculated using:

$$\mu_e = \frac{e}{m_e^*} \frac{\sum_{CB,\boldsymbol{k}} \tau_{n\boldsymbol{k}} f\left(\epsilon_{n\boldsymbol{k}} - \epsilon_f; T\right)}{\sum_{CB,\boldsymbol{k}} f\left(\epsilon_{n\boldsymbol{k}} - \epsilon_f; T\right)} \tag{15}$$

The quotient of the sums gives the thermal averaged relaxation time. The sums run over the lowest conduction band only. Near 0 K, the average relaxation time approaches the relaxation time at the conduction band minimum (CBM) (bottom of the X valley). Mobilities were calculated up to 1000 K. In that temperature range, higher energy conduction bands and the free electron states could be ignored. The value of m_e^* used was the effective Hall mass $m_e^* = 0.67 m_e$ [21].

The average mean free path of electrons was also calculated from the relaxation time using

$$\lambda_{n\boldsymbol{k}} = \left|v_{g,n\boldsymbol{k}}\right| \tau_{n\boldsymbol{k}} \tag{16}$$

where $v_{g,n\boldsymbol{k}}$ are the electron group velocities. These mean free path values were used to assess the degree of localization in the electron-phonon interaction.

3. RESULTS AND DISCUSSIONS

3.1. PHONON DENSITY OF STATES

The calculated phonon dispersion curves of the pristine lattice using a 6×6×6 q-grid are displayed in Figure 1. SiC has two atoms per primitive unit cell, corresponding to six phonon modes, three of which are acoustic modes, and three of which are optical modes. The electron-phonon interaction depends strongly on the polarization of the

phonon modes. For example, the matrix elements of the transverse acoustic modes (TA) are smaller than the longitudinal acoustic mode (LA) because the LA mode produces both shear strain and volume dilation/contraction, while TA modes only produce shear strain [22].

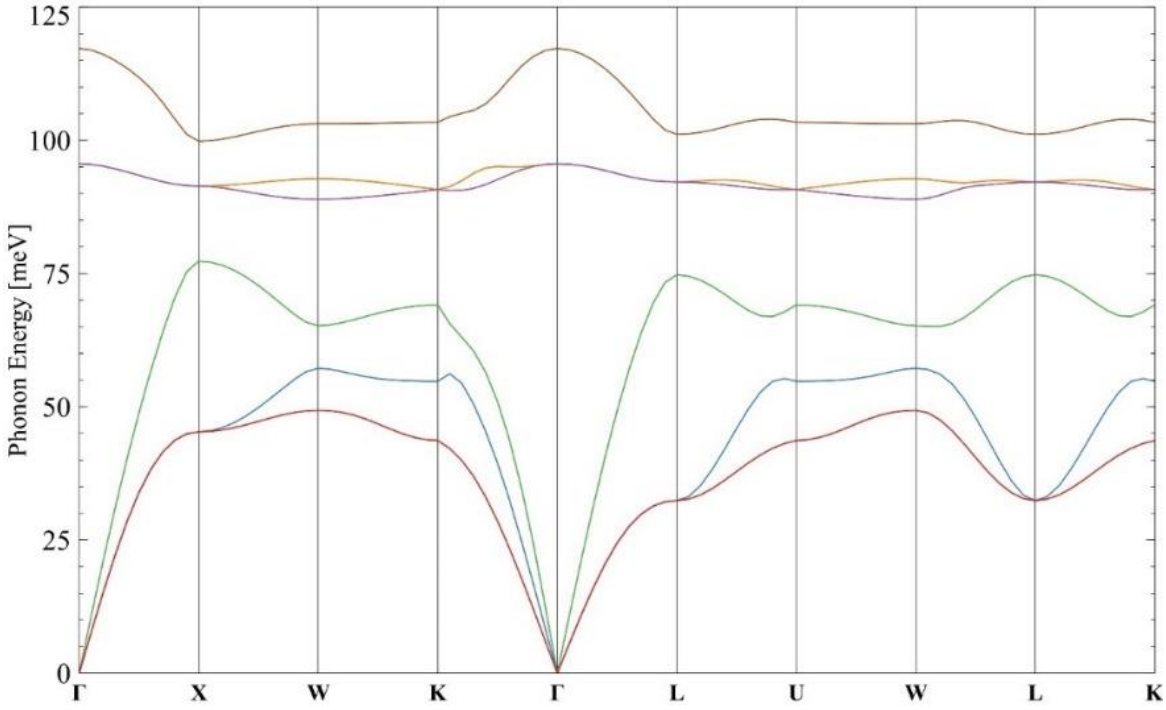

Figure 1: Phonon dispersion curves of pristine 3C-SiC lattice calculated on a 6×6×6

The calculated phonon dispersion curves are in good agreement with inelastic X-ray scattering [23] and Raman scattering [24] measurements. The phonon density of states (DOS) of the pristine lattice using a 6×6×6 q-grid is shown in Figure 2. The high-frequency peaks are mainly associated with vibrations of the lighter carbon atoms, while the lower frequency features tend to have a more mixed character.

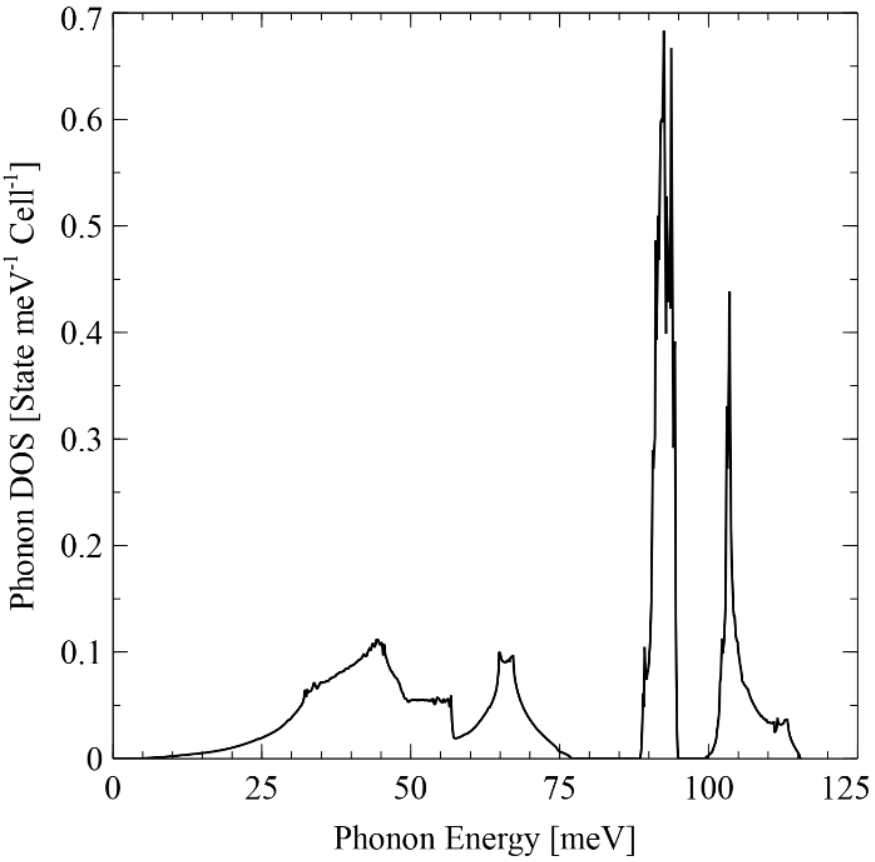

Figure 2: Phonon density of states of the pristine 3C-SiC lattice calculated on a 6×6×6 coarse q-grid

The effect of vacancies on the phonon DOS is illustrated in Figure 3. Both vacancy types cause splitting and the appearance of low energy modes. This is expected from the interruption of long-range order and decrease in the average Si-C bond strength. In $SiC_{0.875}$, there is a greater degree of splitting and a notable down shift in the energies of the optical phonons which is expected as those phonon branches are largely characterized by vibrations on the carbon sublattice.

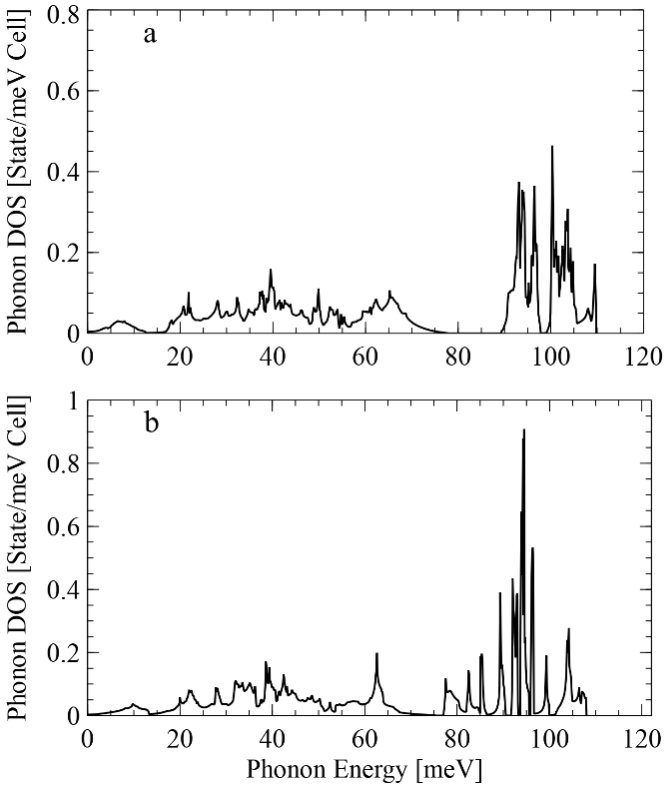

Figure 3: Defective cells phonon density of states (a) Phonon DOS of $Si_{0.875}C$ (b) Phonon DOS of $SiC_{0.875}$ modes were interpolated onto a 12×12×12 coarse q-grid

3.2. ELECTRON BAND STRUCTURE

The electron band structure for pristine 3C-SiC is shown in Figure 4. The corresponding electron DOS is shown in Figure 5. These results show good agreement with the computational literature [25] and experimental literature [26]. Figure 6 shows the electron DOS for $Si_{0.875}C$ and $SiC_{0.875}$.

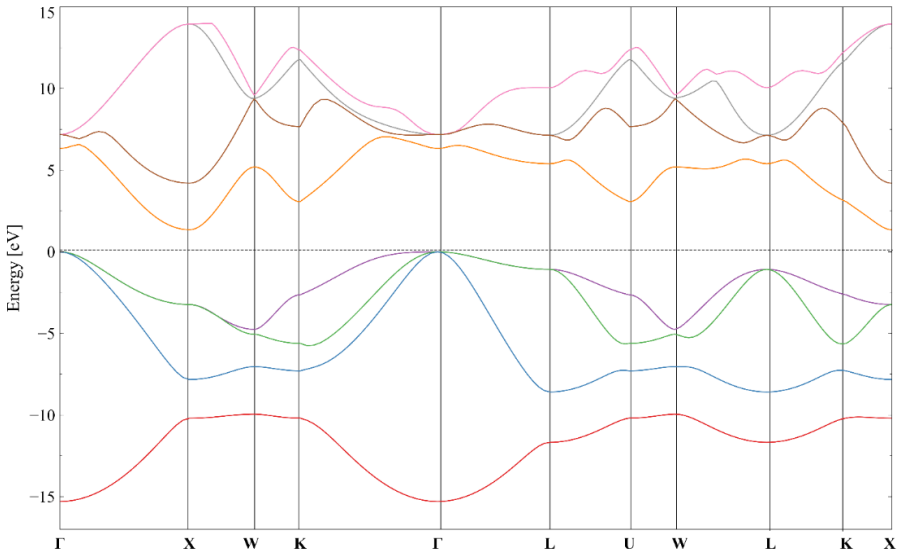

Figure 4: Electron band structure of pristine 3C-SiC. zero energy coincides with the valence band maximum (VBM)

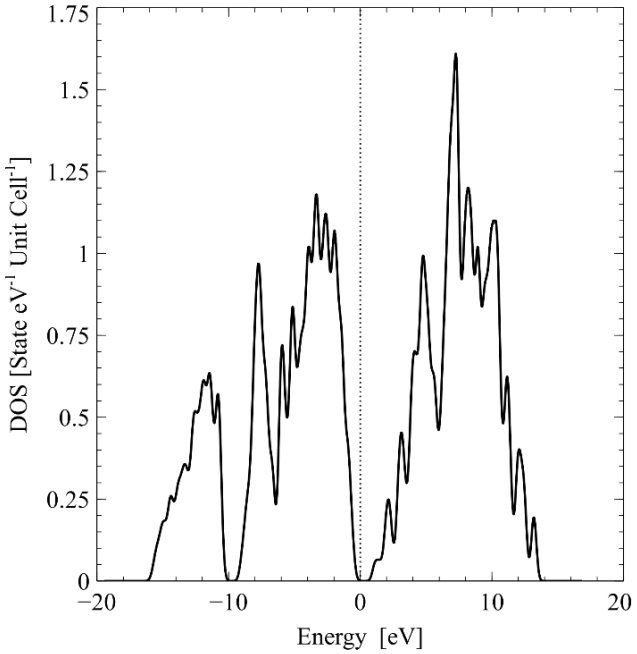

Figure 5: Electron density of states of pristine 3C-SiC

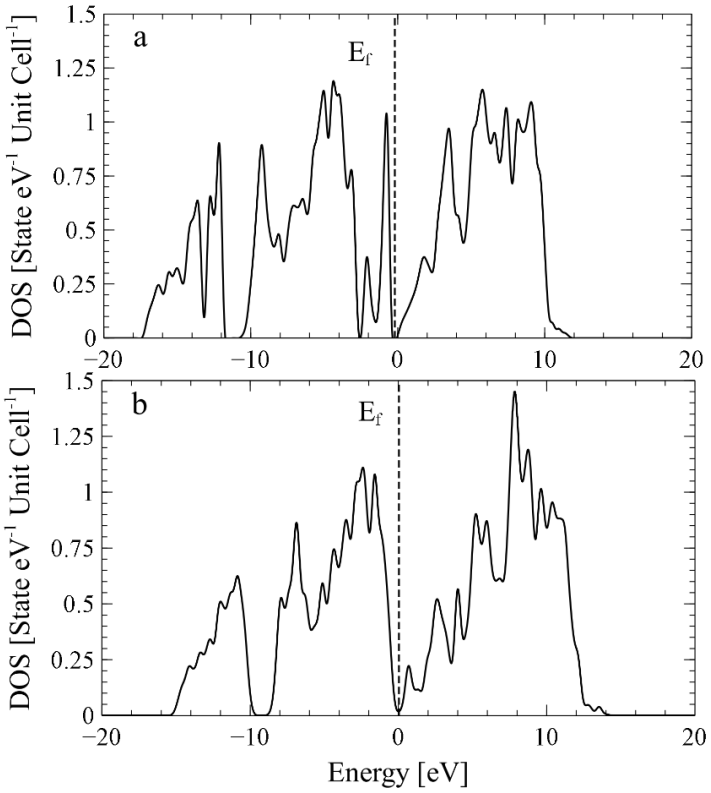

Figure 6: Electronic density of states of defective cells (a) Electronic DOS of $Si_{0.875}C$ (b) Electronic DOS of $SiC_{0.875}$

3.3. ELECTRON-PHONON RELAXATION TIME AND G

Referring to Figure 4, the upper three valance bands (bands 2, 3, and 4) meet at the valence band maximum (VBM) while the conduction band minimum (CBM) occurs in only the lowest conduction band (band 5). Therefore, at low temperatures, those four bands have the greatest contribution to the specific heat capacity, electron-phonon coupling factor and electron mobility. Relaxation times are plotted along a Brillouin zone path in Fig. 7. The three upper valence bands are shown by the dashed red lines while the lowest conduction band is shown by the dotted blue line.

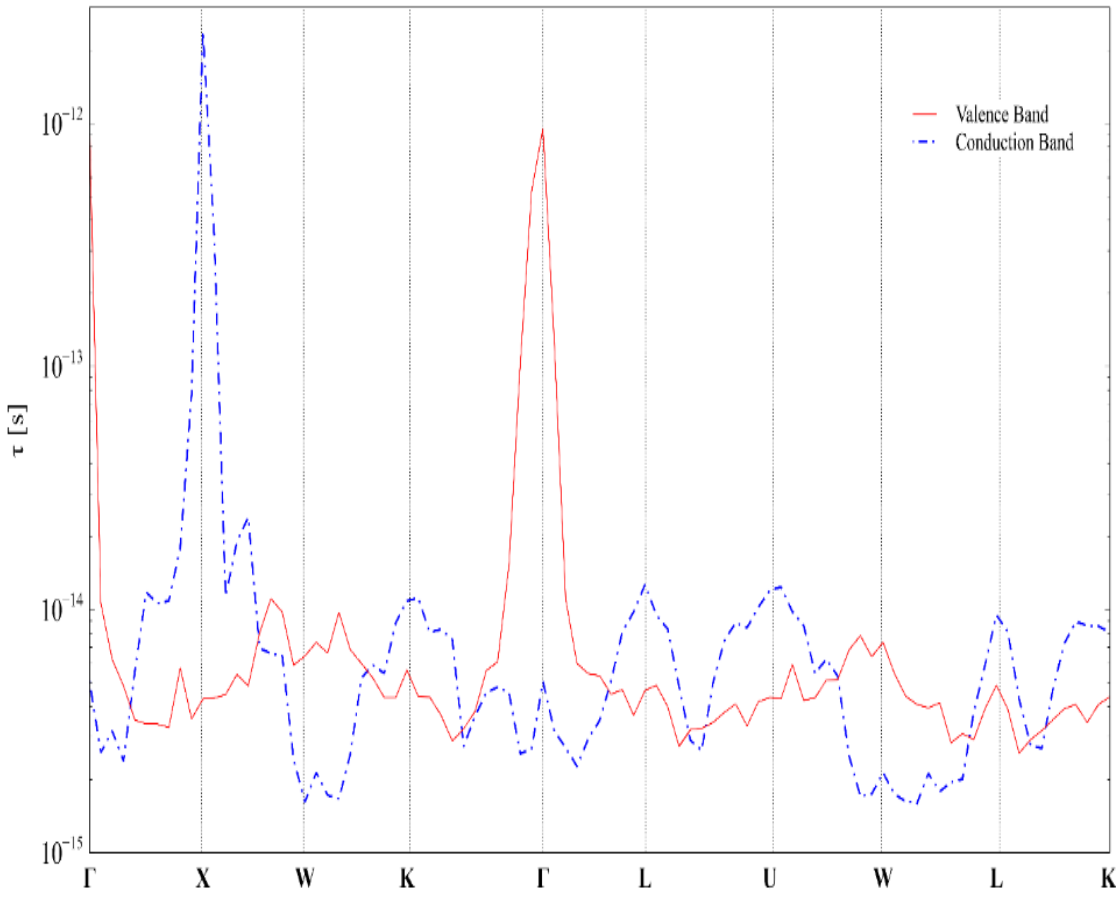

Figure 7: Relaxation times along a Brillouin zone path calculated on a fine 46×46×46 q-grid. The uppermost valence band is shown in red. The lowest conduction band is shown in blue

As expected, the relaxation time of the lowest conduction band is highest at X due to the valley at that point (X valley). The maximum relaxation time for valence electrons occurs at Γ, coinciding with the valence band maximum.

The relaxation times for pristine 3C-SiC are plotted in Figure 8 as a function of the difference in energy between the electron energy level and the Fermi level.

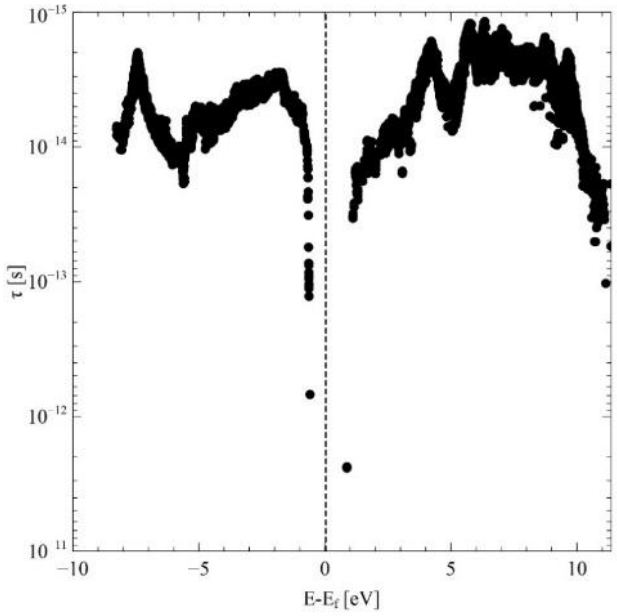

Figure 8: Relaxation time vs. the energy difference from the Fermi level for pristine 3C-SiC at 20 K

As with Figure 7, the longest-lived carriers are found at the VBM and CBM. The CBM electrons lack lower energy states to scatter into. Similarly, holes in the VBM lack higher energy states to scatter into. Meanwhile, in the middle of the bands, the abundance of adjacent states reduces the lifetime to around 10-14 s. The relaxation times also decrease as temperature increases due to the lowering of occupation numbers.

The situation changes when vacancies are added. The narrowing of the bandgap and production of in-gap defect states increases the number of states that conduction electrons near the band edge can scatter down into and valence band holes can scatter up into. Figure 9a shows how the lifetimes of states near the VBM and CBM decrease by several orders of magnitude due to the narrowing of the band gap in Si0.875C (Figure 6). States near the VBM are particularly affected. Figure 9b, which shows the same for $SiC_{0.875}$, indicates less pronounced change in the relaxation time near the VBM.

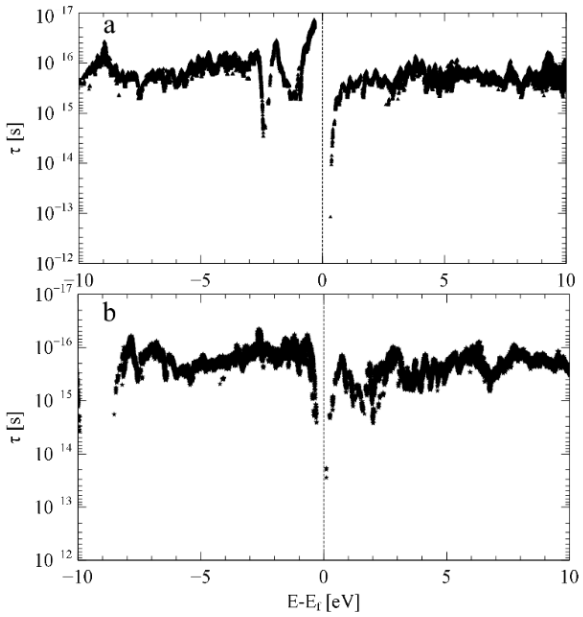

Figure 9: (a) Relaxation time vs. energy in $Si_{0.875}C$ (b) Relaxation time vs. energy in $SiC_{0.875}$

The electronic specific heat capacities calculated using Eqs. 6-9, are shown in Figure 10. At temperatures below 10^5 K, nearly all electrons are accounted for in the static band structure calculations and $n_{free}(T) \cong 0$. At those temperatures, modification of the electronic density of states has a profound effect on the specific heat capacity. In $Si_{0.875}C$, the narrowing of the band gap increases the density of states near the Fermi level. Those states make a greater contribution to the specific heat capacity. In $SiC_{0.875}$, the partial overlap of the bands further increases the density of states near the Fermi level. As the temperature increases, however, the broadening of the Fermi-Dirac distribution smears out the details of the band structure. Also, a larger number of electrons are treated as free electrons. Eventually, at very high temperatures, the heat capacity approaches the classical value for a Maxwell-Boltzmann gas, i.e. $c_v \cong \frac{3}{2} N k_B$, where N is the number of valence electrons per unit volume.

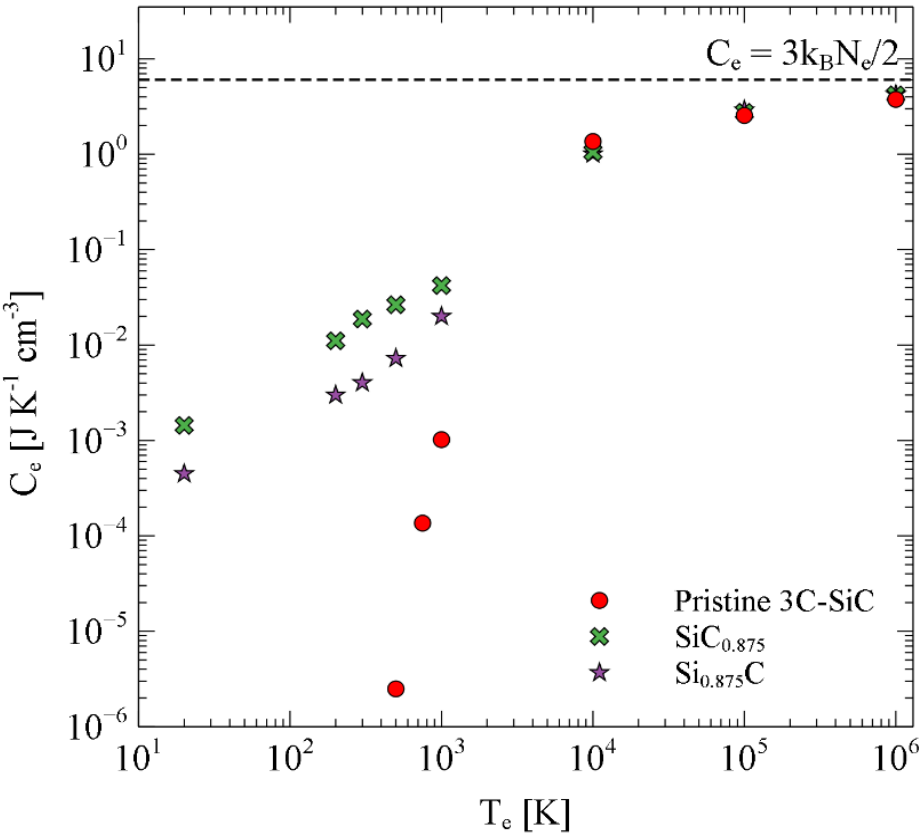

Figure 10: Electronic specific heat capacity as a function of electron temperature.

Using the mode resolved specific heat capacities and relaxation times, the electron-phonon coupling factors were calculated from Eq. 10. The coupling factors are shown in Figure 11. In all cases, G increases as T_e increases. Over all temperatures, the vacancies increase the coupling factor by several orders of magnitude, but the increase is most pronounced at low temperatures. Interestingly, the differences in specific heat and relaxation times between the defective structures seem to largely cancel out. The larger

specific heat for $SiC_{0.875}$ is compensated for by its longer relaxation time. Thus, the values of G are similar for both defective structures over all temperatures.

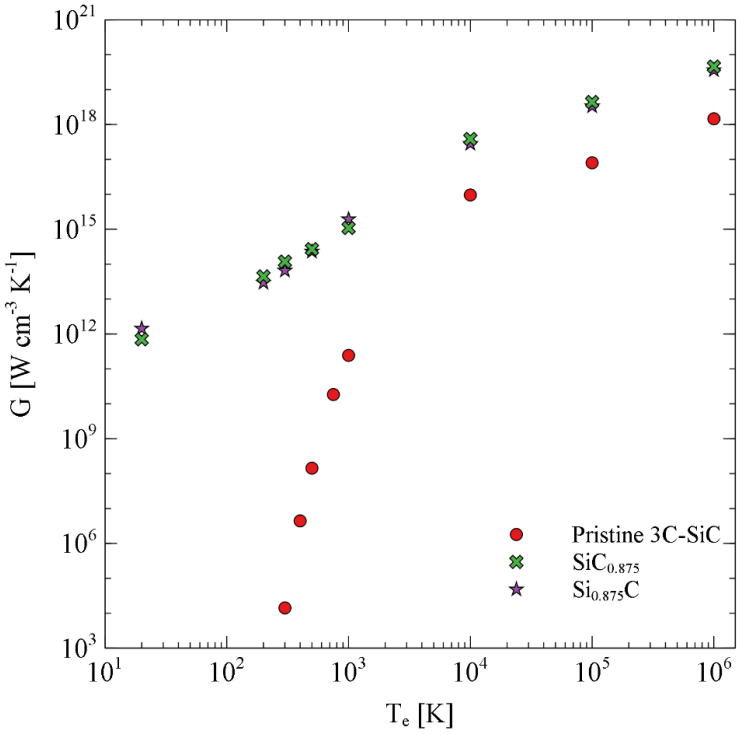

Figure 11: Electron-phonon coupling factor vs. electron temperature for pristine SiC, $SiC_{0.875}$, and $Si_{0.875}C$

The electron mobilities calculated from the relaxation times are compared with the experimental electron Hall mobilities measured in lightly (unintentionally) donor-doped 3C-SiC in Figure 12. [27]. Calculated values from the Caughey-Thomas model [68] are also overlaid. There is reasonably good agreement between the calculations and data when one takes into account the following factors. First, there is inherent variability in Hall measurements due to impurity concentration [27]. These calculations do not consider several relaxation mechanisms such as electron-electron scattering, electron-

dislocation scattering, and electron-impurity scattering. The latter mechanism accounts for the larger differences between the calculated and measured mobilities at 20 K and 50 K. As temperature decreases, the lattice scattering rate decreases while the impurity scattering rate increases [29]. The inflection in the experimental data around 60 K indicates the presence of both impurity and lattice scattering. Since the present calculations do not include the effects of impurities, the higher mobilities at 20 and 50 K are expected. Also note that in the calculations, only the electron temperature is varied. The lattice temperature is fixed at 0 K and therefore, only Stokes processes are accounted for. At elevated temperatures, the anti-Stokes processes should also reduce the electron mobility. Nevertheless, better than order of magnitude agreement was observed in a temperature range where lattice scattering (electron-phonon coupling) is the dominant relaxation mechanism.

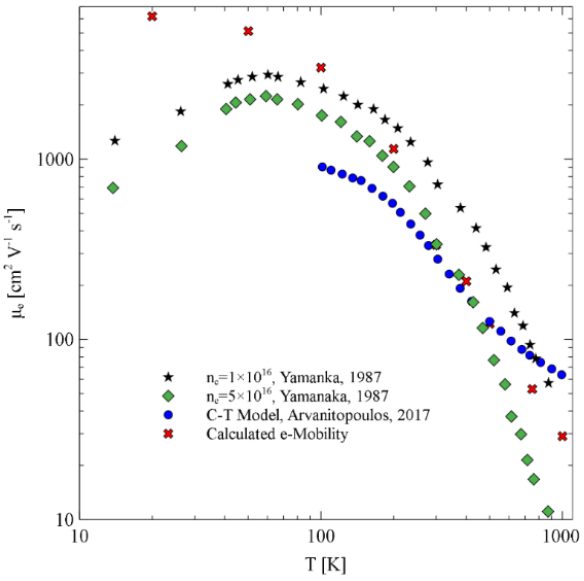

Figure 12: Electron mobilities calculated in the present model (red crosses) along with Hall mobilities measured for lightly doped 3C-SiC taken from [27] and values calculated using the Caughey-Thomas (blue circles) taken from [28]

The mean free paths of electrons calculated using Eq. 15 are shown in Figure 13 as histograms. The main outcome from the calculation is that the mean free paths of electrons in the defective cells are smaller than the lattice parameter at temperatures greater than 200 K. This implies that when electrons scatter in the presence of vacancies, the scattering is highly localized, perhaps occurring over a length scale of an atom or a bond. This suggests that it may be possible to use a rule of mixtures approach in interpolating G over a range of stoichiometries given by SiC_x and Si_xC where $0.875<x<1.0$. Between 20 K and 200 K, there are a small number of states with mean free paths larger than the lattice constant. Since some of those states can carry a significant fraction of the specific heat capacity, it may not be reasonable to use a rule-of-mixtures approach as the interaction can take place over several unit cells.

Interpolation to other stoichiometries may be further complicated by non-linearities in the DOS and band structure. Defective 2×2×2 supercells, though necessary to make the problem computationally tractable, cannot be regarded as a small perturbation to the pristine cell from an isolated vacancy. Figure 6 shows clear narrowing of the band gap and, in the case of $SiC_{0.875}$, a semi-metallic DOS. At much lower defect concentrations, localized defect states are expected to be more-or-less uncoupled and show negligible dispersion (i.e. exhibit flat bands). A 2×2×2 supercell might not provide an accurate approximation of the effect of an isolated point defect on states near E_f. That said, it is clear from comparing Figures 8 and 9 that vacancy defects have a profound effect on the lifetimes of states of all energies within the band structure. Future work will need to be conducted to: 1) validate the rule of mixtures approximation either using larger

supercell calculation or some other approximation and 2) calculate the coupling constant for various stoichiometries and explore its impact on the two-temperature model.

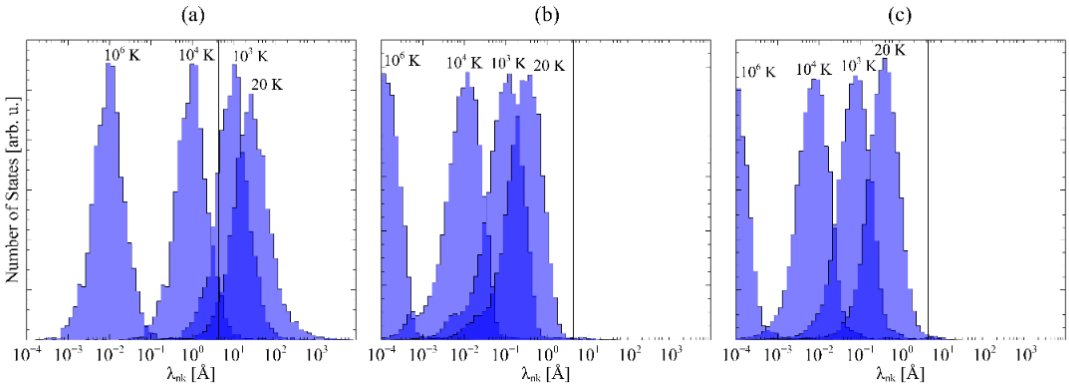

Figure 13: The electron mean free path of (a) pristine cell, (b) $Si_{0.875}C$, and (c) $SiC_{0.875}$. The vertical line corresponds to the lattice constant

4. CONCLUSION

Electron relaxation times, specific heat capacities, electron drift mobilities, electron-phonon coupling factors, and electron-phonon mean free paths were calculated for pristine 3C-SiC, $Si_{0.875}C$, and $SiC_{0.875}$ for electron temperatures from 20 K to 10^6 K. The calculations were performed using a hybrid model which combines density functional perturbation theory calculations with a free electron gas model. The model was validated by comparing calculated electron mobilities with measured Hall mobilities.

Vacancy defects have a profound effect on the electron specific heat capacity at low temperatures due to changes in the electron density of states near the Fermi level. The relaxation times decrease and the electron-phonon coupling factors increase by several orders of magnitude in the defective structures compared to pristine 3C-SiC. Both

vacancy types have nearly the same magnitude of effect on the coupling factor. Perhaps most importantly, the coupling factor strongly depends on the electron temperature. Such temperature dependence is not usually accounted for in the two-temperature model. While an effective electron-phonon coupling *constant* has been used as a fitting parameter within the two-temperature model to successfully explain experimental data from swift heavy ion irradiations and pulsed laser experiments, the consequences of the strong temperature dependence on the coupling factor should be investigated further.

Electron-phonon mean free paths calculated in the defective supercells were found to be, in most cases, much smaller than the lattice constant. This suggests that it may be possible to interpolate the electron-phonon coupling factors to other stoichiometries of SiC using a simple rule-of-mixtures approach. This will need to be confirmed by either performing the calculations in a larger supercell, in effect lowering the vacancy concentration, or through an alternative approach.

ACKNOWLEDGMENT

The authors thank the Information Technology teams of the Missouri University of Science and Technology and University of Missouri-Columbia for their help and support. This work was supported in part by U.S. Nuclear Regulatory Commission Faculty Development Grant NRC-HQ-84-15-G-0044.

AUTHOR DECLARATION

CONFLICT OF INTEREST

The authors have no conflicts to disclose.

DATA AVAILABILITY

The data that support the findings of this study are available from the corresponding author upon reasonable request.

REFERENCES

[1] W. J. Kim, D. Kim, and J. Y. Park, Nucl. Eng. Technol. **45**, 565 (2013). doi: 10.5516/NET.07.2012.084.

[2] T. Wang, Z. Gui, A. Janotti, and C. Ni, Phys. Rev. Mater. **1**, 034601 (2017). doi: 10.1103/PhysRevMaterials.1.034601.

[3] Y. Katoh and L. L. Snead, J. Nucl. Mater. **526**, 151849 (2019). doi: 10.1016/j.jnucmat.2019.151849.

[4] Z. Wang, W. E. I. Liu, and C. Wang, J. Electron. Mater. **45**, 267 (2016). doi: 10.1007/s11664-015-4107-8.

[5] S. K. Srivastava and D. K. Avasthi, Def. Sci. J. **59**, 425 (2009). doi: 10.14429/dsj.59.1542.

[6] J. A. Alonso and N. H. March, Electrons in Metals and Alloys, (Academic Press, San Diego, 1989) pp. 129–203, doi: 10.1016/b978-0-12-053620-7.50009-3.

[7] S. Savrasov and D. Savrasov, Phys. Rev. B **54**, 16487 (1996). doi: 10.1103/PhysRevB.54.16487.

[8] M. S. Tyagi and R. Van Overstraeten, Solid State Electron. **26**, 577 (1983). doi: 10.1016/0038-1101(83)90174-0.

[9] Y. Zhang, T. Varga, M. Ishimaru, P.D. Edmondson, H. Xue, P. Liu, S. Moll, F. Namavar, C. Hardiman, S. Shannon, and W.J. Weber, Nucl. Instrum. Meth. B **327**, 33 (2014). doi: 10.1016/j.nimb.2013.10.095.

[10] Q. Xu, J. Zhou, T. H. Liu, and G. Chen, Appl. Phys. Lett. **115**, 023903 (2019). doi: 10.1063/1.5108836.

[11] M. Toulemonde, E. Paumier, and C. Dufour, Rad. Eff. Defect. S. **126**, 201 (1993). doi: 10.1080/10420159308219709

[12] A. Meftah, J.M. Costantini, N. Khalfaoui, S. Boudjadar, J.P. Stoquert, F. Studet, and M. Toulemonde, Nucl. Instrum. Meth. B, **237**, 563 (2005). doi: 10.1016/j.nimb.2005.02.025.

[13] S. L. Daraszewicz, and D. M. Duffy, Nucl. Instrum. Meth. B **269**, 1646 (2010). doi: 10.1016/j.nimb.2010.11.031

[14] M. J. Verstraete, J. Phys. Condens.-Mat. 25, 136001 (2013). doi: 10.1088/0953-8984/25/13/136001.

[15] P. Ji and Y. Zhang, Phys. Lett. A. 380, 1551 (2016). doi: 10.1016/j.physleta.2016.02.044.

[16] M. Calandra and F. Mauri, Phys. Rev. B. 76, 1 (2007). doi: 10.1103/PhysRevB.76.205411.

[17] P Giannozzi, O. Andreussi, T. Brumme, O. Bunau, M. Buongiorno Nardelli, M. Calandra, R. Car, C. Cavazzoni, D. Ceresoli, M. Cococcioni, J. Phys. Condens.-Mat. 29, 65901 (2017). doi: 10.1088/1361-648X/aa8f79.

[18] G. Pizzi, V. Vitale, R. Arita, S. Blüge, F. Freimuth, G. Géranton, M. Gibertini, D. Gresch, C. Johnson, T. Koretsune, J. Phys. Condens.-Mat. 32 , 165902 (2020). doi:10.1088/1361-648x/ab51ff.

[19] S. Poncé, E.R. Margine, C. Verdi, F. Giustino, EPW: Electron–phonon coupling, transport and superconducting properties using maximally localized Wannier functions,Computer Physics Communications, 209, 116, (2016).doi: 10.1016/j.cpc.2016.07.028.

[20] F. Schindler, J. Geilker, W. Kwapil, W. Warta, and M. C. Schubert, J. Appl. Phys. 110, 043722 (2011). doi: 10.1063/1.3622620.

[21] C. Persson and U. Lindefelt, Phys. Rev. B **54**, 10257 (1996). doi: 10.1103/PhysRevB.54.10257.

[22] N. Tandon, J. D. Albrecht, and L. R. Ram-Mohan, J. Appl. Phys. **118**, 045713 (2015). doi: 10.1063/1.4927530.

[23] J. Serrano, J. Strempfer, and M. Cardona, Appl. Phys. Lett. **80**, 4360 (2002). doi: 10.1063/1.1484241.

[24] D. W. Feldman, J. H. Parker, Jr., W. J. Choyke, and L. Patrick, Phys. Rev. **173**, 787 (1968).

[25] G. L. Zhao and D. Bagayoko, New J. Phys. **2**, 16 (2000). doi: 10.1088/1367-2630/2/1/316.

[26] A. R. Lubinsky, D. E. Ellis, and G. S. Painter, Phys. Rev. B. **11**, 1537 (1975).

[27] M. Yamanaka, H. Daimon, E. Sakuma, S. Misawa, and S. Yoshida, J. Appl. Phys. **61**, 599 (1987). doi: 10.1063/1.338211.

[28] A. Arvanitopoulos, N. Lophitis, K. N. Gyftakis, S. Perkins, and M. Antoniou, Semicond. Sci. Technol. **32**, 104009 (2017). doi: 10.1088/1361-6641/aa856b.

[29] C. Kittel, Introduction to Solid State Physics, 2nd Ed. (John Wiley and Sons, New York, 1956) pp. 361-365

II. THE TEMPERATURE-VARIABLE ELECTRON-PHONON COUPLING AND ITS ROLE IN THE INELASTIC THERMAL SPIKE IN 3C-SiC

Salah Al Smairat, Joseph Graham

Department of Nuclear Engineering and Radiation Science
Missouri University of Science and Technology, Rolla, MO 65409

ABSTRACT

In Two Temperature Model calculations of the inelastic thermal spike produced by the passage of a swift ion, it is common practice to treat the electron-phonon coupling factor as a constant. However, recent first principles calculations in 3C-SiC have shown that the electron-phonon coupling factor is strongly dependent on the electron temperature. The evolution of the electron and phonon temperatures were calculated using both an electron-temperature-variable electron-phonon coupling as well as constant couplings. The maximum electron and phonon temperatures were compared for different electronic stopping powers and at different radii from the ion path. While the use of constant couplings appears to be somewhat justified for certain combinations of radius and stopping power, the high energy densities at the center of ion paths formed by high stopping power swift heavy ions are capable of greatly enhancing the coupling, sometimes by several orders of magnitude. This work shows that some of the physical assumptions of the Two Temperature Model must break down near the center of the ion path.

1. INTRODUCTION

Silicon carbide is a technologically important ceramic. It has numerous uses which take advantage of its hardness, large thermal conductivity, low coefficient of thermal expansion, semiconducting properties, and radiation tolerance [1-3]. In the nuclear industry, SiC is used as a coating in Tri-Isostructural (TRISO) fuel, where it provides crush resistance and acts as a fission product barrier [4]. SiC is being incorporated into Accident Tolerant Fuel (ATF) concepts in light water reactors and as a structural material in the flow channels of fusion systems [4-6].

Owing to its importance in the nuclear industry, radiation effects in SiC have been the subject of decades of research [7]. Both electronic and nuclear energy loss mechanisms should be included in a full description of primary radiation damage. For example, the primary knock-on atoms (PKA) produced by elastic collisions from fission spectrum neutrons lose a significant fraction of their energy from both electronic energy loss and nuclear energy loss. Fission fragments on the other hand, lose the majority of their energy through electronic energy loss. To an appreciable extent, the coupling between the electronic system and lattice governs the formation of microstructural features by the passage of swift heavy ions. Depending on the ion energy and mass, partially amorphous broken tracks, fully amorphous tracks, local phase changes, and defect annealing have been observed in various materials. Excitation of the electronic system and its coupling to the lattice can be understood through the inelastic Thermal Spike (i-TS) model [8,9].

In the i-TS model, an ion passes through the solid, ionizing and ejecting energetic electrons (delta electrons). Those electrons then thermalize within femtoseconds through electron-electron interactions resulting in the formation of a hot electron-hole plasma. The electron-hole plasma begins to diffuse away from the center of the ion trajectory and while doing do, transfers energy to the lattice through the electron-phonon coupling. The size and duration of the of the thermal spike in the lattice and its cooling rate influence the resulting microstructure. One such microstructural phenomenon observed in SiC is swift heavy ion beam induced epitaxial recrystallization (SHIBIEC) [10,11]. In SHIBIEC, swift heavy ions anneal preexisting defects produced by nuclear energy loss (elastic collisions). This is seen when SiC samples are irradiated by two different ion beams, one with a low electronic to nuclear stopping ratio, and a second with a high ratio [12].

The Two Temperature Model (TTM), which arose out of research on pulsed laser irradiation, provides a mathematical description of the i-TS. It assumes that electrons and atoms constitute two different subsystems, each with a well-defined temperature. The governing equations are a pair of coupled heat equations with a volumetric energy source term in the electronic equation [8].

$$C_e \frac{\partial T_e}{\partial t} = \nabla \cdot [k_e \nabla T_e] - G(T_e - T_{ph}) + A(r,t) \quad (1)$$

$$C_{ph} \frac{\partial T_{ph}}{\partial t} = \nabla \cdot \left[k_{ph} \nabla T_{ph}\right] + G(T_e - T_{ph}) \quad (2)$$

The subscripts ‘e’ and ‘ph’ denote the parameters for electrons and phonons, respectively. C_i are the volumetric heat capacities, k_i are the thermal conductivities, G is

the electron phonon coupling factor, and $A(r,t)$ is the radial- and time-dependent electronic energy deposition source term from the ion. G can be regarded as a constant fitting parameter or it can be estimated from the electron-phonon relaxation time (τ_{e-ph}) and heat capacity [13],

$$G = \frac{C_e}{\tau_{e-ph}} \tag{3}$$

Eq. 8 can be derived from the Boltzmann transport equation in the constant relaxation time approximation. It is known that in semiconductors and insulators, electronic heat capacity, electrical resistivity, and conductivity can depend strongly on temperature. Given that the electronic temperatures predicted by the TTM can vary by more than tens of thousands of degrees, the use of a constant coupling factor is questionable. Indeed, previous calculations of this factor using Density Functional Perturbation Theory (DFPT) [14] show a rather dramatic dependence on electronic temperature as shown in Figure 1.

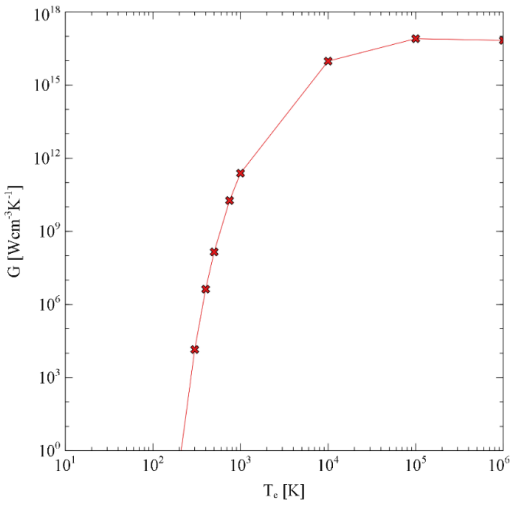

Figure 1: Electron phonon coupling factor, G, vs. electron temperature [14]

In this study, TTM calculations of the electron and phonon temperatures were carried out over a range of electronic stopping powers from 2.3 – 15.2 keV nm^{-1}, with a fixed specific energy of 1 MeV u^{-1}. Two implementations of the electron-phonon coupling were compared. In one, the electron-phonon coupling was allowed to vary as a function of electron temperature according to the data shown in Figure 1. In the second approach, the electron-phonon coupling was treated as a constant.

2. METHODOLOGY

Two Temperature Model calculations were performed on a 1D cylindrically and axially symmetric grid. The calculations were implemented using the FiPy finite volume PDE solver [15]. A uniform radial mesh and logarithmic time steps were used. The source term in Eq. 1, was based on the formula of Katz et al. [16] with Waligorski et al.'s empirical correction factor [17] and using Fageeha et al.'s density correction [18]. Time dependence was implemented using a simple exponential decay function, i.e.,

$$A(r,t) = D(r)\,\frac{1}{\tau_{e-e}}\,e^{-\frac{t}{\tau_{e-e}}} \tag{4}$$

is an electron-electron relaxation time, taken to be 10-15 s. The values of the phonon heat capacity and thermal conductivity were obtained from the literature [1,6]. The electronic volumetric heat capacity and electronic thermal diffusivity were assumed to be 1 J cm^{-3} K and 2 cm2 s^{-1} respectively, which is based on the argument that hot electrons in semiconductors and insulators behave like hot electrons in metals [19].

25 °C was used as the initial temperature and as Dirichlet boundary conditions for the outer surface of the domain. The initial time step was 10-17 s and was incremented

logarithmically by 0.1% per step. Simulations performed with constant couplings used values of 1012, 1013, 1014, 1015, and 1016 W cm-3 K-1. At the melting point of SiC, an additional heat loss term was incorporated into Eq. 2, to account for the latent heat of fusion.

3. RESULTS AND DISCUSSIONS

The maximum electronic temperature vs. electronic stopping power are shown in Figure 2 for radii of 0.5, 2.5, 5.5, and 10.5 nm away from the center of the ion path. Each curve corresponds to a different prescription for the electron-phonon coupling.

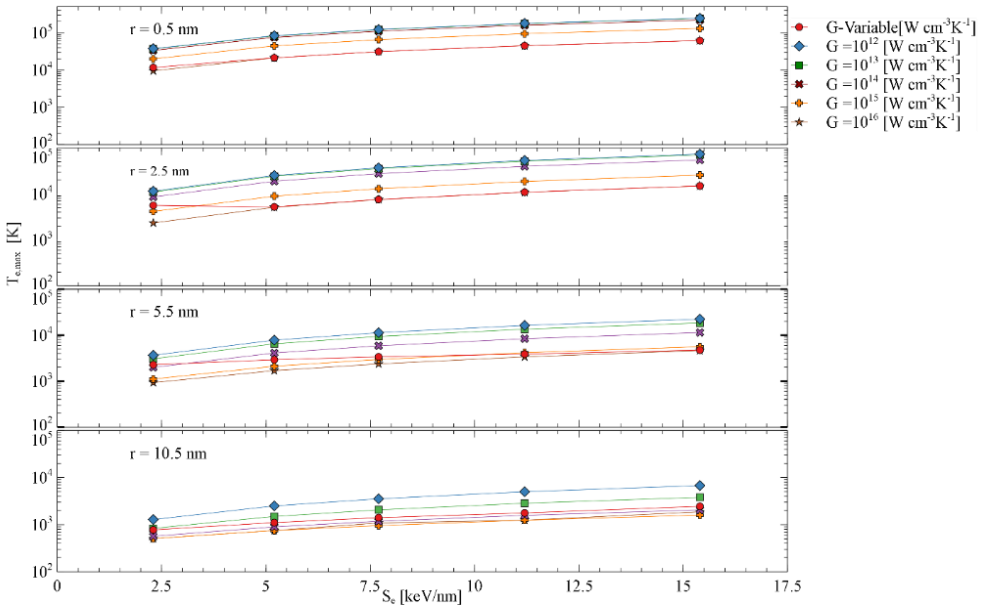

Figure 2: Maximum electron temperature vs. stopping power at different radii from the center of the ion path. The specific ion energy is fixed at 1 MeV u^{-1}

Figure 3 shows the time evolution of the electronic temperature for stopping powers of 2.3 and 15.4 keV nm^{-1} at radii of 0.5 and 10.4 nm.

Considering both Figures. 2 and 3, the effective electron phonon coupling that best reproduces the variable coupling at the center of the track is between 10^{15} and 10^{16} $Wcm^{-3}K^{-1}$. In the case of lower stopping powers (Figures 3(a) and (c)) this value decreases rapidly with radius, down to between 10^{12} and 10^{13} W cm^{-3} K^{-1}. Those lower values are comparable to similar couplings used in TTM calculations for SiC [20,21]. An interesting double peak feature is seen at the larger radius (Figure 3(c) and (d)) at higher couplings. This is due to rapid initial coupling followed by a delayed, diffusion limited coupling as hot electrons from the core region diffuse outwards.

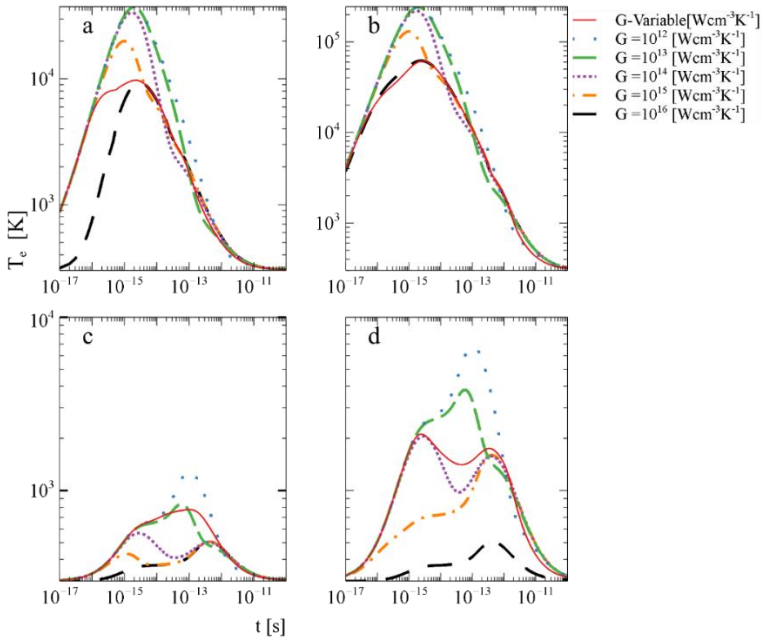

Figure 3: Electronic temperature vs. time curves (a) 0.5 nm from the center of the ion path, Se=2.3 keV/nm, (b) 0.5 nm from center, Se=15.2 keV/nm, (c) 10.5 nm from center, Se = 2.3 keV/nm, and (d) 10.5 nm from center, Se = 15.2 keV/nm

The maximum lattice temperatures vs. stopping power curves are shown in Figure 4 Corresponding temperature vs. time curves are shown in Figure 5 Similar qualitative behavior is seen with lattice temperature as with electron temperature. Interestingly, even at moderately low electronic stopping powers, the melting point of 3C-SiC (~3000 K) can be exceeded within a few nm. Comparison of the lattice temperature vs. time curves in Figure 5, however, show that the temperature fall back below the melting point within one picosecond, even at the highest stopping powers. Considering that the phonon frequencies of SiC extend over a few tens of THz [22], it is unlikely that enough atomic vibrations will have occurred for any significant amount of atomic rearrangement to take place resulting in track melting. In other words, the formation of observable ion tracks appears to be kinetically unlikely. On the other hand, the rather large lattice temperatures and localized heat deposition predicted by the variable coupling might help explain the SHIBIEC phenomena. On timescales where defects can hop, the local lattice temperature can still be a significant fraction of the melting point, providing the thermal energy needed to help anneal said defects.

These results underscore several limitations of the TTM, at least in its use with SiC. Much of the variation in the lattice temperature occurs over timescales where atoms are essentially frozen. It is therefore unlikely that the atomic system will be able to explore a sufficiently large number of microstates to make the concept of a latent heat of fusion physically meaningful. Perhaps more importantly, at the center of the ion path, temperature changes occur over timescales less than fs. Over these timescales, the assumption of well-defined electron and phonon temperatures is no longer valid as the delta electrons have not fully thermalized and produced an equilibrium electron-hole

plasma. In other words, the electronic system begins to couple to the atomic system before electrons can establish quasi-thermal equilibrium. To properly understand energy transfer at the center of the ion trajectory, it will be necessary to shift to a Boltzmann Transport framework, which incorporates high energy electron-phonon scattering events. The electron-temperature-variable electron-phonon coupling used in this work itself is based on several simplifying assumptions about thermal equilibrium. Therefore, it will need to be replaced with electron momentum dependent electron-phonon scattering cross sections. Nevertheless, at radii sufficiently far away from the center of the ion path and at low enough stopping powers, the use of the TTM and an effective coupling constant appear to be justifiable.

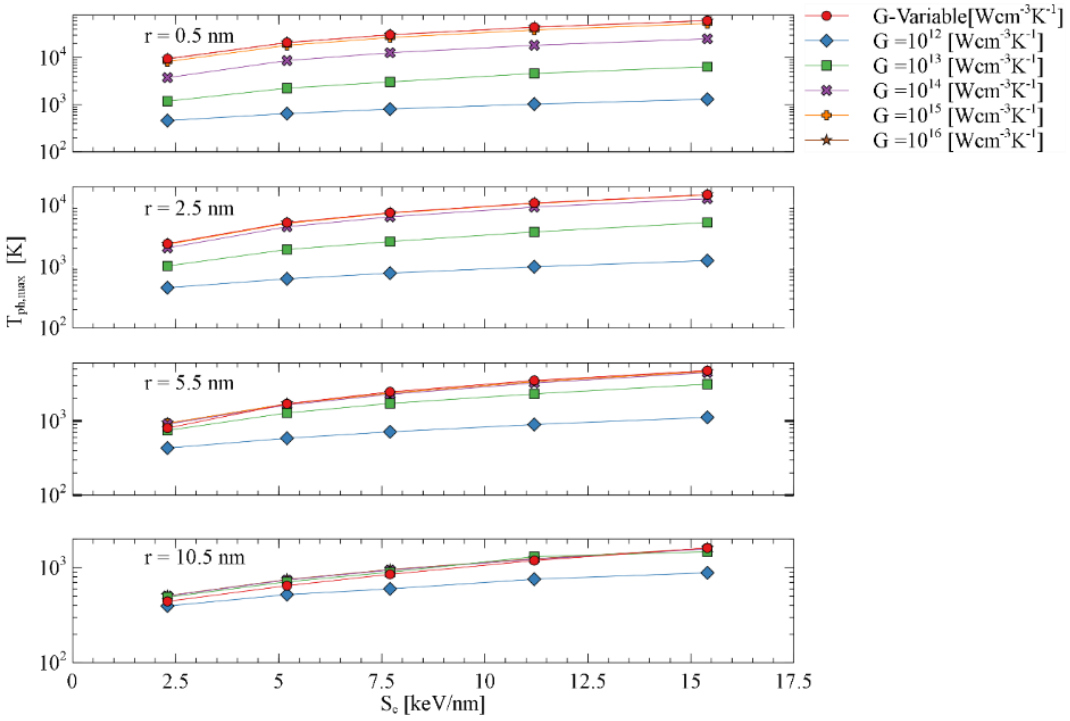

Figure 4: Maximum phonon (lattice) temperature vs. stopping power at different radii from the center of the ion path

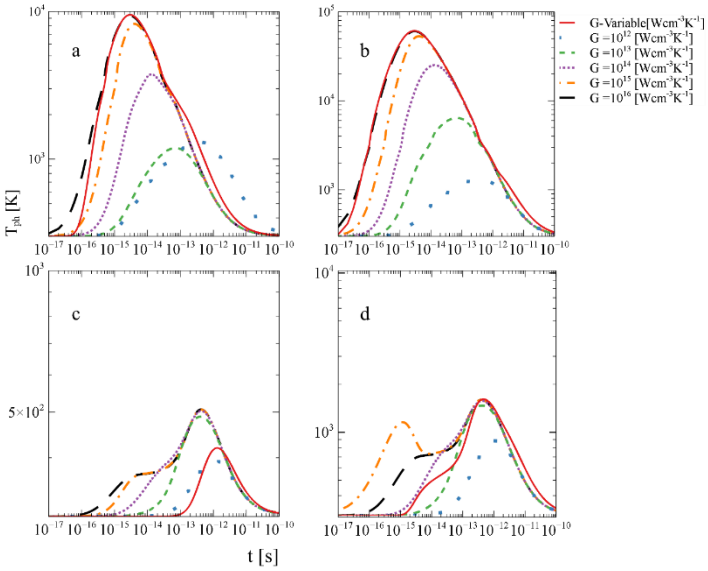

Figure 5: Phonon (lattice) temperature vs. time curves (a) 0.5 nm from the center of the ion path, S_e=2.3 keV/nm, (b) 0.5 nm from center, S_e=15.2 keV/nm, (c) 10.5 nm from center, S_e = 2.3 keV/nm, and (d) 10.5 nm from center, S_e = 15.2 keV/nm

4. CONCLUSION

Two Temperature Model calculations of the inelastic thermal spike resulting from the passage of swift heavy ions in 3C-SiC were performed. Several prescriptions for the electron-phonon coupling elucidated the complex electron and lattice temperature evolution near the center of the ion trajectory. An electron-temperature-variable coupling factor shows intense coupling at the center of the ion path, corresponding to an effective coupling constant of up to 10^{16} W cm^{-3} K^{-1} that rapidly decreases to 10^{12}-10^{13} W cm^{-3} K^{-1} several nm away from the center. Though the calculations predict lattice temperatures well in excess of the melting point of SiC, those temperatures exist over timescales too short to allow for track melting. This is in agreement with previous TTM calculations and experimental evidence that show that ion tracks do not form in SiC. The results do,

however, illustrate some of the limitations of the TTM. To fully describe energy transfer near the center of the ion path, it will be necessary to relax the assumption of well-defined electron and lattice temperatures and adopt a Boltzmann transport approach.

ACKNOWLEDGMENT

The authors thank the Information Technology teams of the Missouri University of Science and Technology and University of Missouri-Columbia for their help and support. This work was supported in part by U.S. Nuclear Regulatory Commission Faculty Development Grant NRC-HQ-84-15-G-0044.

AUTHOR DECLARATIONS

CONFLICT OG INTEREST

The authors have no conflicts to disclose.

DATA AVAILABILITY

The data that support the findings of this study are available from the corresponding author upon reasonable request.

REFERENCES

[1] T. Wang, Z. Gui, A. Janotti, C. Ni, and P. Karandikar, “Strong effect of electron-phonon interaction on the lattice thermal conductivity in 3C-sic”, *Physical Review Materials*, vol. 1, no. 3, 2017, doi: https://doi.org/10.1103/PhysRevMaterials.1.034601

[2] Z. Wang, W. Liu, and C. Wang, “Recent progress in ohmic contacts to silicon carbide for high-temperature applications”, *J. Electron. Mater.*, vol. 45, no. 1, pp. 267–284, 2016, doi: https://doi.org/10.1007/s11664-015-4107-8

[3] S. J. Zinkle, J. W. Jones, and V. A. Skuratov, “Microstructure of swift heavy ion irradiated SiC, Si3N4 and AlN”, *MRS Proceedings*, vol. 650, p. R3.19, 2000, doi: https://doi.org/10.1557/PROC-650-R3.19

[4] Y. Katoh and L. L. Snead, “Silicon carbide and its composites for nuclear applications – Historical overview”, *J. Nucl. Mater.*, vol. 526, no. 151849, p. 151849, 2019, doi: https://doi.org/10.1016/j.jnucmat.2019.151849

[5] W. J. Kim, D. Kim, and J. Y. Park, “FABRICATION AND MATERIAL ISSUES FOR THE APPLICATION OF SiC COMPOSITES TO LWR FUEL CLADDING,Nuclear Engineering and Technology”, *Nucl. Eng. Technol.*, vol. 45, Issue 4, 2013, doi: https://doi.org/10.5516/NET.07.2012.084

[6] R.A. Verrall, M.D. Vlajic, V.D. Krstic, “Silicon carbide as an inert-matrix for a thermal reactor fuel”, *J. Nucl. Mater.*, vol. 274, no. 1–2, pp. 54–60, 1999, doi: https://doi.org/10.1016/S0022-3115(99)00089-6

[7] L.L. Snead, Y. Katoh, T. Nozawa, "Radiation Effects in SiC and SiC-SiC”, *Comprehensive Nuclear Materials*, vol. 4, pp. 215-240, 2020, doi: http://dx.doi.org/10.1016/B978-0-08-056033-5.00093-8

[8] M. Toulemonde, E. Paumier, and C. Dufour, “Thermal spike model in the electronic stopping power regime”, *Radiation Effect and Defects in Solids*, vol. 126, pp. 201-206, 1993, doi: https://doi.org/10.1080/10420159308219709

[9] A. Meftah et al., “Experimental determination of track cross-section in Gd3Ga5O12 and comparison to the inelastic thermal spike model applied to several materials”, *Nucl. Instrum. Methods Phys. Res. B*, vol. 237, no. 3–4, pp. 563–574, 2005, doi: http://dx.doi.org/10.1016/j.nimb.2005.02.025

[10] A. Benyagoub and A. Audren, “Mechanism of the swift heavy ion induced epitaxial recrystallization in predamaged silicon carbide”, *J. Appl. Phys.*, vol. 106, no. 8, 2009, doi: https://doi.org/10.1063/1.3236627

[11] A. Debelle et al., “Combined experimental and computational study of the recrystallization process induced by electronic interactions of swift heavy ions with silicon carbide crystals”, Phys. Rev. B Condens. Matter Mater. Phys., vol. 86, no. 10, 2012, doi: http://dx.doi.org/10.1103/PhysRevB.86.100102

[12] Y. Zhang et al., “Competing effects of electronic and nuclear energy loss on microstructural evolution in ionic-covalent materials”, *Nucl. Instrum. Methods Phys. Res. B*, vol. 327, pp. 33–43, 2014, doi: https://doi.org/10.1016/j.nimb.2013.10.095

[13] S. L. Daraszewicz and D. M. Duffy, “Extending the inelastic thermal spike model for semiconductors and insulators”, *Nucl. Instrum. Methods Phys. Res. B*, vol. 269, no. 14, pp. 1646–1649, 2011, doi: https://doi.org/10.1016/j.nimb.2010.11.031

[14] S. Al Smairat and J. Graham, “Vacancy-induced enhancement of electron–phonon coupling in cubic silicon carbide and its relationship to the two-temperature model”, *J. Appl. Phys.*, vol. 130, no. 12, p. 125902, 2021, doi: https://doi.org/10.1063/5.0056244

[15] J. E. Guyer, D. Wheeler, and J. A. Warren, “FiPy: Partial differential equations with python”, *Comput. Sci. Eng.*, vol. 11, no. 3, pp. 6–15, 2009, doi: 10.1109/MCSE.2009.52

[16] R. Katz, D. E. Dunn, and G. L. Sinclair, “Thin down in Radiobiology”, *Radiation Protection Dosimetry*, vol. 13, Issue 1-4, pp. 281, 1985.

[17] M. P. R. Waligórski, R. N. Hamm, and R. Katz, “The Radial Distribution of Dose around the Path of a Heavy Ion in Liquid Water”, *International Journal of Radiation Applications and Instrumentation. Part D. Nuclear Tracks and Radiation Measurements*, vol. 11, pp. 309, 1986, doi: https://doi.org/10.1016/1359-0189(86)90057-9

[18] O. Fageeha, J. Howard, and R. C. Block, “Distribution of Radial Energy Deposition around the Track of Energetic Charged Particles in Silicon”, *J. Appl. Phys.*, vol. 75, no. 5, pp. 2317–2321, 1994, doi: https://doi.org/10.1063/1.356274

[19] I. A. Baranov, Y. V. Martynenko, S. O. Tsepelevich, and Y. N. Yavlinskiĭ, “Inelastic sputtering of solids by ions”, *Sov. phys. Uspekhi*, vol. 31, no. 11, pp. 1015–1034, 1988, doi: https://doi.org/10.1070/PU1988v031n11ABEH005646

[20] O. Ochedowski et al., “Graphitic nanostripes in silicon carbide surfaces created by swift heavy ion irradiation”, *Nat. Commun.*, vol. 5, no. 1, p. 3913, 2014, doi: https://doi.org/10.1038/ncomms4913

[21] M. Backman et al., “Molecular dynamics simulations of swift heavy ion induced defect recovery in SiC”, *Comput. Mater. Sci.*, vol. 67, pp. 261–265, 2013, doi: http://dx.doi.org/10.1016/j.commatsci.2012.09.010

[22] D. W. Feldman, J. H. Parker, W. J. Choyke, and L. Patrick, “Phonon Dispersion Curves by Raman Scattering in SiC, Polytypes3C,4H,6H,15R, and21R”, *Phys. Rev.*, vol. 173, no. 3, pp. 787–793, 1968, doi: https://doi.org/10.1103/PhysRev.173.787

SECTION

3. UNDERSTANDING THE TEMPERATURE DEPENDENCE OF THE ELECTRON-PHONON COUPLING IN INSULATORS AND METALS: A TIGHT BINDING APPROACH

3.1. OUTLINE

A simple phenomenological model is here developed to help elucidate the key factors influencing the observed behavior of the electron phonon coupling factor presented in papers I and II. One of the more unexpected behaviors is the strong dependence on electronic temperature in 3C-SiC. This model will show that this dependence is largely an effect of band structure bonding. It shows that metals and insulators tend to behave quite differently.

3.2. 1D TIGHT BINDING MODEL

We start with the Tight Binding Model (TBM). This is a standard model used to understand various phenomena in solid state physics such as the electronic structure of insulators, electrical conductivity, and Metal-Insulator Transitions[48]. For simplicity's sake, the 1-dimensional TBM will be used. Only same-site and nearest-neighbor interactions are considered. In a Wannier basis, with a single localized Wannier orbital, the Tight Binding Hamiltonian can be written as[49].

$$\widehat{H}_{TB} = \sum_{n'} |n'+1\rangle t\langle n'| + |n'-1\rangle t\langle n'| + |n'\rangle U\langle n'| \tag{1}$$

$|n'\rangle$ is the Wannier orbital localized at atomic site n', of which there are N sites. t is the hopping integral. It is a measure of the rate of electron hopping from one lattice site to a nearest neighbor (see Figure 3.1a). U is the energy of an electron on a lattice site. Working in the Wannier basis with a single band leads to a number of simplifications. The Bloch states can be written as

$$|k\rangle = \frac{1}{\sqrt{N}} \sum_{n'} e^{ikn'a} |n'\rangle \tag{2}$$

where k is the wavevector and a is the lattice constant (in this case, also the interatomic spacing). Also, the Wannier functions form an orthonormal basis.

$$\langle n|n'\rangle = \delta_{nn'} \tag{3}$$

It is straightforward to show that the eigen energies of the above Hamiltonian are given by

$$\varepsilon_k = U + 2t \cos ka \tag{4}$$

If we assume that the bandwidth is large enough relative to the temperatures of interest (i.e. $k_B T \ll 4t$), one can also approximate the energy momentum relation as[50]

$$\varepsilon_k \approx \varepsilon_0 + \frac{\hbar^2 k^2}{2m} \tag{5}$$

m is the electron effective mass. From this point onward $\varepsilon_0 = 0$, establishing the zero of energy. All other energy parameters such as the chemical potential will be measured relative to it.

3.3. ELECTRON PHONON COUPLING IN THE TIGHT BINDING MODEL

The electron-phonon coupling is incorporated into the 1D TBM in a phenomenological way. Figure. 3.1b shows the effect of moving an atom on the hopping integral terms. Hopping is generally faster when atoms are closer together and slower when atoms are further apart. Thus, the effect of moving atom n closer to $n+1$ (and further away from atom $n-1$) is to increase t by a small amount Δt. This also decreases t by the same amount for hopping between atoms n and $n-1$. The use of a single value of Δt can be justified given the additional assumption that the system is symmetric on flipping the order of the atoms (mirror symmetry).

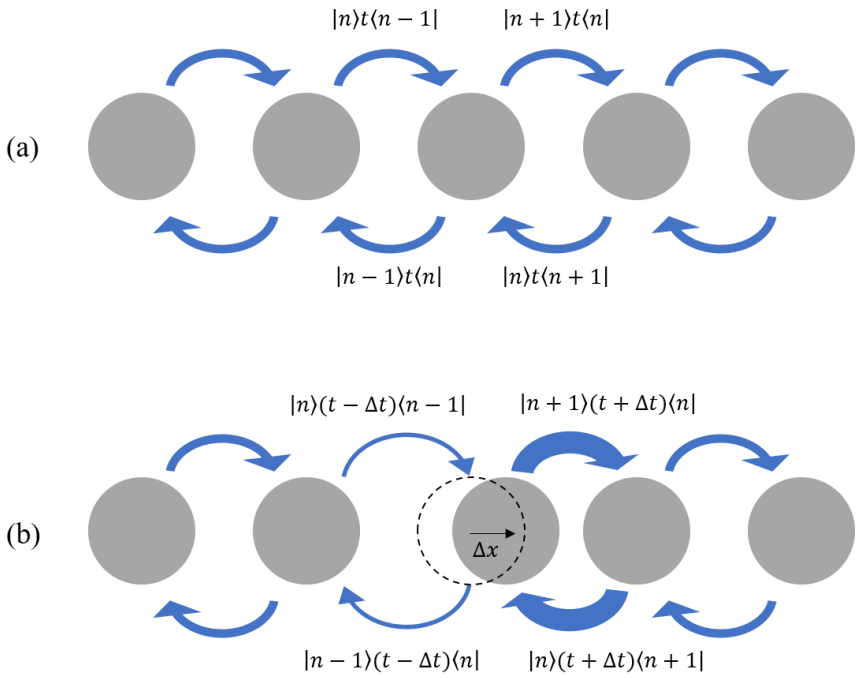

Figure 3.1. 1D Tight bonding model illustration (a) Hopping integral, (b) The effect of moving an atom on hopping integral

The above addition leads to a perturbation of the Hamiltonian of the form

$$\Delta\hat{V}_{epc,n} = \Delta t(|n+1\rangle\langle n| - |n-1\rangle\langle n| + |n\rangle\langle n+1| - |n\rangle\langle n-1|) \tag{6}$$

Here, it is assumed that only atom n is moved. If t is assumed to be a continuous function of the atomic displacement a small displacement of the atom gives the perturbation

$$\begin{aligned}\Delta\hat{V}_{epc,n} \approx \Delta x_n \frac{dt}{dx}(&|n+1\rangle\langle n| - |n-1\rangle\langle n| + |n\rangle\langle n+1| \\ &- |n\rangle\langle n-1|)\end{aligned} \tag{7}$$

Inserting the Bloch states (Eq. 2), the deformation potential is obtained.

$$\begin{aligned}&\langle k'|\partial_n\hat{V}_{epc,n}|k\rangle \\ &\quad= \frac{dt}{dx}\frac{1}{N}\left[e^{-ik\prime(n+1)a}e^{ikna} - e^{-ik'(n-1)a}e^{ikna}\right. \\ &\quad\left.+ e^{-ik'na}e^{ik(n+1)a} - e^{-ik\prime na}e^{ik(n-1)a}\right] \\ &\quad= \frac{dt}{dx}\frac{1}{N}2ie^{-i(k'-k)na}[\sin ka - \sin k'a]\end{aligned} \tag{8}$$

If we assume that the Bloch state energies span a range of several eV but the electrons gain and lose energy through the absorption and emission of phonons with only a few meV of energy, it is reasonable to approximate the sine terms with a simple difference.

$$\langle k'|\partial_n\hat{V}_{epc,n}|k\rangle \approx \frac{dt}{dx}\frac{1}{N}2ie^{-i(k'-k)na}(k-k')a \tag{9}$$

Lastly, the phonons are treated using Einstein model, i.e. all atoms vibrate independently with frequency ω_0. This leads to a flat phonon dispersion curve. It also simplifies the integral of the electron scattering rate (Eq. 4 in Paper I). Rather than summing over all phonon wavevectors, the sum can be performed over the N atoms.

$$\frac{1}{\tau_k} = \frac{2\pi}{\hbar}\sum_n \int \frac{dk'}{\Omega_{BZ}} |g_n(k',k)|^2[(1-f_{k'})\delta(\varepsilon_k - \varepsilon_{k'} - \hbar\omega_0) + f_{k'}\delta(\varepsilon_k - \varepsilon_{k'} + \hbar\omega_0)] \tag{10}$$

where

$$g_n(k',k) = \langle k'|\partial_n \hat{V}_{epc,n}|k\rangle \tag{11}$$

Here, the Bose factor is ignored as we are assuming hot electron coupling to a cold lattice near 0 K. Because we assume all atoms are equivalent, the sum is replaced by N.

$$\frac{1}{\tau_k} = \frac{2\pi}{\hbar}\int \frac{dk'}{\Omega_{BZ}} N|g_n(k',k)|^2[(1-f_{k'})\delta(\varepsilon_k - \varepsilon_{k'} - \hbar\omega_0) + f_{k'}\delta(\varepsilon_k - \varepsilon_{k'} + \hbar\omega_0)] \tag{12}$$

Making use of Eq. 5

$$\frac{1}{\tau_k} = \frac{4a^3}{\hbar}\left(\frac{dt}{dx}\right)^2 \int dk'\,(k-k')^2\left[(1-f_{k'})\delta\left(\frac{\hbar^2k^2}{2m} - \frac{\hbar^2k'^2}{2m} - \hbar\omega_0\right) + f_{k'}\delta\left(\frac{\hbar^2k^2}{2m} - \frac{\hbar^2k'^2}{2m} + \hbar\omega_0\right)\right] \tag{13}$$

Then using the composition rule for delta functions

$$\frac{1}{\tau_k} = \frac{4a^3}{\hbar}\left(\frac{dt}{dx}\right)^2 \int dk'\,(k-k')^2\left[(1-f_{k'})\frac{m}{\hbar^2|k'|}\left\{\delta\left(k' + \sqrt{k^2 - \frac{2m\omega_0}{\hbar}}\right) + \delta\left(k' - \sqrt{k^2 - \frac{2m\omega_0}{\hbar}}\right)\right\} + f_{k'}\frac{m}{\hbar^2|k'|}\left\{\delta\left(k' + \sqrt{k^2 + \frac{2m\omega_0}{\hbar}}\right) + \delta\left(k' - \sqrt{k^2 + \frac{2m\omega_0}{\hbar}}\right)\right\}\right] \tag{14}$$

Separating the Stokes and Anti-stokes terms gives

$$\left(\frac{1}{\tau_k}\right)_{stokes} = \frac{4ma^3}{\hbar^3}\left(\frac{dt}{dx}\right)^2\left[\frac{\left(k-\sqrt{k^2-\frac{2m\omega_0}{\hbar}}\right)^2}{\sqrt{k^2-\frac{2m\omega_0}{\hbar}}}\right. \\ \left. + \frac{\left(k+\sqrt{k^2-\frac{2m\omega_0}{\hbar}}\right)^2}{\sqrt{k^2-\frac{2m\omega_0}{\hbar}}}\right](1-f_{k\prime}) \tag{15}$$

$$\left(\frac{1}{\tau_k}\right)_{antistokes} = \frac{4ma^3}{\hbar^3}\left(\frac{dt}{dx}\right)^2\left[\frac{\left(k-\sqrt{k^2+\frac{2m\omega_0}{\hbar}}\right)^2}{\sqrt{k^2+\frac{2m\omega_0}{\hbar}}}\right. \\ \left. + \frac{\left(k+\sqrt{k^2+\frac{2m\omega_0}{\hbar}}\right)^2}{\sqrt{k^2+\frac{2m\omega_0}{\hbar}}}\right]f_{k\prime} \tag{16}$$

After additional simplification we arrive at

$$\left(\frac{1}{\tau_k}\right)_{stokes} = \frac{16\sqrt{2m}ma^3}{\hbar^4}\left(\frac{dt}{dx}\right)^2\frac{\varepsilon_k-\frac{\hbar\omega_0}{2}}{\sqrt{\varepsilon_k-\hbar\omega_0}}\left(1 \right. \\ \left. - \frac{1}{1+\exp\left(\beta(\varepsilon_k-\hbar\omega_0-\mu)\right)}\right) \tag{17}$$

$$\left(\frac{1}{\tau_k}\right)_{antistokes} = \frac{16\sqrt{2m}ma^3}{\hbar^4}\left(\frac{dt}{dx}\right)^2\frac{\varepsilon_k+\frac{\hbar\omega_0}{2}}{\sqrt{\varepsilon_k+\hbar\omega_0}}\left(\frac{1}{1+\exp(\beta(\varepsilon_k+\hbar\omega_0-\mu))}\right) \tag{18}$$

where $\beta^{-1} = k_B T$ and μ is the electron chemical potential. Reusing the electronic heat capacity and definition of the electron phonon coupling factor (Eqs. 3 and 7 in Paper I), we have

$$C(\varepsilon_k) = k_B \beta^2 \frac{(\varepsilon_k - \mu)^2 \exp(\beta(\varepsilon_k - \mu))}{[1 + \exp(\beta(\varepsilon_k - \mu))]^2} \tag{19}$$

$$G(\varepsilon) = \frac{C(\varepsilon)}{\tau(\varepsilon)} \tag{20}$$

Rather than summing over all wavevectors all terms can be conveniently written in terms of electron energy. Therefore, one can simply integrate the energy-resolved coupling $G(\varepsilon)$ with the electron density of states. On a 1D lattice with parabolic dispersion, the density of states is

$$D(\varepsilon) \propto \frac{1}{\sqrt{\varepsilon}} \tag{21}$$

Therefore, the temperature-dependent coupling can be evaluated using

$$G(T) \propto \int D(\varepsilon) G(\varepsilon)\, d\varepsilon \tag{22}$$

3.4. CALCULATIONS OF G(Te) FOR METALS AND INSULATORS

If we ignore the constant coefficients in Eqs. 19 and 20, G is only parameterized by the phonon energy $\hbar\omega_0$, the chemical potential μ, and the electron temperature T. Setting $\hbar\omega_0$=10 meV we can compare the temperature dependence of G for an insulator and a metal. This is accomplished by setting $\mu = -0.5$ eV for the insulator and $\mu = 0.5$ eV for the metal. In the case of the insulator. The chemical potential will fall below the lowest energy state (which we regard as the conduction band minimum) and lie in the

equivalent of the band gap. In the case of the metal, the chemical potential will fall in the middle of a band resulting in a partially filled band with a Fermi surface. Though the parabolic band extends to infinite energy, a 1.5 eV cutoff is imposed on the integrals. This acts as an effective bandwidth. Though the use of the TBM with nearest-neighbor-only interactions is inappropriate for metals, the purpose of this phenomenological model is to merely to illustrate how large of an effect band structure and bond type can have on the electron phonon coupling.

The coupling factors for both the metal and insulator are shown in Figure 3.2. As was the case with 3C-SiC the 1D insulator has a dramatic temperature dependence, changing coupling over several orders of magnitude. The metal, on the other hand, increases more gradually with temperature and shows comparatively weak temperature dependence. This is in agreement with previous first-principles calculations for metals [51][52][53].

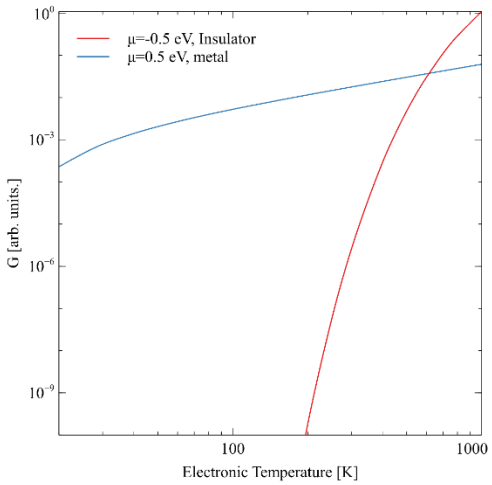

Figure 3.2: Electron-phonon coupling constant vs. electronic temperature for metals (blue line), and insulators (red line)

Because the bandwidth, effective mass, and hopping integrals were held fixed, the large difference between these curves must be a result of the difference in bonding. In the case of metallic bonding, only electrons near the Fermi surface participate in energy transfer with the lattice. As temperature increases, electrons within $\hbar\omega_0$ of the Fermi surface are surrounded by an increasing number of unoccupied states into which they can scatter. However, the occupation numbers do not change as dramatically as a function of temperature near the Fermi surface as away from the Fermi surface. In contrast, in the insulator, the conduction electrons are present at a low concentration and the levels are mostly unfilled. Thus, there are many more states for electrons to scatter into. At the same time, the heat capacity is much more strongly dependent on temperature as the population of conduction electrons mostly depends on the high energy "tail" of the Fermi-Dirac distribution. That tail, being approximately a decaying exponential, has an area that varies exponentially over temperature.

The above conclusions show that the calculated electron-phonon coupling will depend sensitively on the assumptions made about the statistical distribution of electrons produced following ion impact. In papers I and II, it was assumed that the energy distribution of electrons and holes is governed by a single temperature and Fermi-Dirac statistics are valid. In the literature on the Two Temperature Model (TTM), it is sometimes assumed (but not always explicitly stated) that a degenerate electron gas forms in the conduction band where it behaves as a metal. In the latter case, the parameters of the TTM alone are insufficient to fully describe the relevant physics. At a minimum, the carrier concentration must also be considered in addition to the electron temperature. It

may even be necessary to consider electron and holes has having two different temperatures.

Given the apparent importance of the statistical distribution of electrons in the electron-phonon coupling in insulators, a final factor which should be considered is recombination. Two recombination mechanisms can influence the statistical distribution of hot electrons in insulators. Auger recombination is a process that scales as the cube of the carrier density [54]. It is observed at high electronic excitation densities, such as those produced by pulsed laser irradiation [55][56]. Under those conditions is a fast process that can potentially contribute to the establishment of a well-defined electronic temperature and Fermi-Dirac distribution. On the other hand, Auger recombination is known to depend strongly on the width of the band gap and on the dielectric constant. Shockley-Read-Hall (SRH) recombination, on the other hand, is a slower, trap-assisted recombination mechanism. If recombination was limited by the SRH process, it is conceivable that electrons and holes would separately form degenerate gases in the conduction and valence bands, and the electron-phonon coupling could have a temperature dependence more similar to a metal. For a degenerate gas to form, however, the electronic excitation density would have to be large enough to fill a significant number of states near the conduction band minimum. On the other hand, at high electronic excitation densities, Auger recombination becomes more significant.

In summary, the phenomenological model presented in this chapter helps explain the dramatic temperature dependence of the electron phonon coupling predicted in 3C-SiC and the comparatively weak dependence in metals. At the same time, it raises many additional questions that can likely only be answered through detailed simulations of the

Boltzmann Transport Equation. Those simulations should consider: Auger recombination and its dependence on electronic excitation density and stopping power; Shockley Read Hall recombination; evolution of the energy distribution of electrons and holes and establishment of electron (and hole) temperatures; and dependence of the electron phonon coupling on the aforementioned distribution and its behavior in the regime of low and high electronic excitation density and in regimes dominated by Auger recombination and Shockley Read Hall recombination.

4. CONCLUSIONS AND RECOMMENDATIONS

4.1. SUMMARY AND CONCLUSION

The electron-phonon coupling in 3C-SiC was investigated. The effect of electronic temperature on the magnitude of the coupling was studied as was the effect of vacancy point defects. Calculations of the coupling factor employed a hybrid method utilizing *ab-initio* methods and a classical electron gas model to account for high energy electrons. In the first paper, the electron relaxation time was calculated for pristine and defective SiC using the quantum chemistry codes, Quantum Espresso and Electron-Phonon using Wannier functions (EPW). Mode resolved relaxation times ($\tau_{n\boldsymbol{k}}$), and the electronic heat capacity (C_e) were calculated for different electron temperatures. Through the relaxation time τ, and the heat capacity, the electron-phonon coupling were calculated at each temperature. The calculations were validated using measured electron Hall mobilities. The electron-phonon coupling in 3C-SiC was found to be strongly temperature-dependent, and strongly affected by point defects. These effects have not

been adequately investigated before. A main contribution of the first paper was to show how wide a range of coupling factors can exist in the same material, at different electronic temperatures, and in the presence of defects.

In the second paper, the electronic temperature-dependent electron-phonon coupling was incorporated into the Two Temperature Model. Calculations of the electron and lattice temperatures following impact from a swift heavy ion were modeled for different stopping powers. Upon comparison to results obtained using constant values of the coupling, significant differences were seen. It was observed that at the center of the ion track, the electron phonon coupling is strong (on the order of 10^{16} W cm^{-3} K^{-1}) but decreases rapidly as a function of radius from the center of the track. The evolution of electron and lattice temperatures over time were quite different. For the variable coupling, energy transfer starts within 10^{-15} s. Given that electron thermalization takes place over similar time scales, it seems that these results illustrate a breakdown of the TTM. The TTM assumes that the electrons reach quasi-thermal equilibrium before significant heat transfer to the lattice can occur. At the center of the track, the effective coupling is evidently strong enough that thermalization and electron-phonon coupling may be competing processes. In future analyses, it may be necessary to analyze the dynamics through the Boltzmann transport equation which does not assume well-defined electron and phonon temperatures.

The main contributions of this dissertation are:

1. This was the first work to use first principles methods to calculate the electron-phonon coupling in pristine and defective SiC.

2. A hybrid method was developed to calculate electron phonon coupling factors in semiconductors and insulators from cryogenic temperatures to extreme high temperatures.
3. It was shown that the assumption of a constant electron phonon coupling in the two-temperature model is not valid in general.

4.2. FUTURE WORK

Several suggestions for future work are summarized below:

1. Although calculations of the electron phonon coupling were performed in small supercells with very high concentration of defects, those results might be interpolated to lower concentrations. In the defective cells, calculated electron-phonon mean free paths were found to be smaller, sometimes much smaller, than a lattice constant. This suggests that the electron-phonon coupling near a defect is highly localized. Thus, a simple rule-of-mixtures approach might be used to interpolate the coupling to more dilute defect densities. Results of the rule-of-mixtures should be benchmarked against calculations using larger supercells (e.g. 3×3 or 4×4) to determine whether or not the use of rule-of-mixtures is appropriate.
2. For the sake of computational speed, all calculations were performed in the Local Density Approximation. An unintended consequence of using the LDA is an inaccurate prediction of the band gap. Though computationally more expensive, Generalized Gradient Approximation (GGA) DFT calculations could provide more accurate band structure calculations. Comparison to the

LDA results could also help elucidate the role of the band gap in the electron phonon coupling.

3. Semiconductors other than SiC can be investigated. Silicon, germanium, and gallium arsenide share similarities in structure but also have differences in electronic structure and electrical properties.
4. The Boltzmann Transport Equation (BTE) could be solved with the scattering rates or matrix element developed the first part of this work to better model the inelastic thermal spike in situations where quasi-thermal equilibrium is not yet established.
5. For completeness, the effects of other point defects such as self-interstitial atoms and anti-sites on the electron phonon coupling in SiC should be studied.

APPENDIX

PYTHON CODE

```
from fipy.tools import numerix
import scipy
import fipy
import numpy as np
from fipy import CylindricalGrid1D
from fipy import Variable, CellVariable, TransientTerm,
DiffusionTerm, Viewer, LinearLUSolver, LinearPCGSolver, \
    LinearGMRESSolver, ImplicitDiffusionTerm, Grid1D,\
ImplicitSourceTerm

# Mesh
nr = 1000
dr = 1e-7
mesh = CylindricalGrid1D(nr=nr, dr=dr, origin=0)

# Variables
T_e = CellVariable(name="electronTemp", mesh=mesh,\
hasOld=True)
T_e.setValue(300)
T_ph = CellVariable(name="phononTemp", mesh=mesh,\
hasOld=True)
T_ph.setValue(300)
G = CellVariable(name="EPC", mesh=mesh)
x = mesh.cellCenters[0]
t = Variable()

# Material parameters
C_e = CellVariable(name="C_e", mesh=mesh)
K_e = CellVariable(name="k_e", mesh=mesh)
L = CellVariable(name="Latent heat", mesh=mesh)
C_ph = CellVariable(name="C_ph", mesh=mesh)
K_ph = CellVariable(name="k_ph", mesh=mesh)

# Gaussian parameters for latent heat
a = 0.75
sig2 = 600
L = a * numerix.exp(-(T_ph - 3103)**2 / (2 * sig2**2))
```

```
# Coefficients
C_e = 2.342/(1 + (T_e/8.78e3)**-2.7685)
C_ph = 4.10446 - 3.886 * numerix.exp(-T_ph / 373.8) + L
K_e = 2   # W/cm K
K_ph = (4.681e-2 + 8.044e-2 * T_ph)/(1 - 1.155e-2 * T_ph \
+ 1.018e-4 * T_ph**2)
G = numerix.exp(0.012 * (numerix.log(T_e))**3 -\
0.6291*(numerix.log(T_e))**2 + 11.105*numerix.log(T_e) - \
22.848)
#G = 1e14

# Boundary conditions
T_e.constrain(300, where=mesh.facesRight)
T_ph.constrain(300, where=mesh.facesRight)
tau = 1e-15

##### Wlgorski Source
D_1 = CellVariable(name="source", mesh=mesh)
D_2 = CellVariable(name="source3", mesh=mesh)
D_t = CellVariable(name="source1", mesh=mesh)
K_1 = CellVariable(name="source2", mesh=mesh)
E = 207   #rgy in mev
M = 207  # %mass in amu
Z = 82  #;
N = 9.66e23  # %Electron density in e/cc
dens = 3.21   #; %Density
B = 0.215
beta = numerix.sqrt(2*E/M/931.5)
C = 3.127 - 0.434 * beta
Zp = Z*(1 - numerix.exp(-125 * beta * Z**(-2/3)))
e2 = 1.44e-10  #; %keVcm
mc2 = 511

if beta < 0.0081:
    A = 0
elif 0.0081 < beta < 0.091:
    A = 112*beta - 0.899
elif beta > 0.091:
    A = 0.674*beta + 9.21
K_1 = A * (beta**B) * (x * 1e7 - 0.1) * numerix.exp(-x\
*1e7/C)
N = 9.66e23
W = 2*mc2 * (beta**2) /(1 - beta**2)
I = 0.072   #keV
k = 1.86e-6  #1.869e-6
```

```
if I < 1:
    alpha = 1.079
elif I > 1:
    alpha = 1.667

theta = k * (I**alpha)
if W < 1:
    alpha2 = 1.079
elif W > 1:
    alpha2 = 1.667

T = k * W**alpha2
D_1 = 1.6e-16 * ((N * e2**2 * Zp**2)/(x *
alpha*mc2*beta**2))*(((1((x+theta)/(T+theta)))**(1/alpha))\
          (x+theta))
D_2 = np.where(np.isnan(D_1), 0, D_1)
D_t = D_2 * (1 + K_1)
A_r = D_t * tau**-1 * numerix.exp(-t / tau)

##### Equations
eq0 = (TransientTerm(var=T_e, coeff=C_e) ==
DiffusionTerm(var=T_e, coeff=K_e) - \
       ImplicitSourceTerm(coeff=G, var=T_e) +\
 ImplicitSourceTerm(var=T_ph, coeff=G) +  A_r)

eq1 = (TransientTerm(var=T_ph, coeff=C_ph) ==
DiffusionTerm(var=T_ph, coeff=K_ph) +
ImplicitSourceTerm(var=T_e, coeff=G) -
ImplicitSourceTerm(coeff=G, var=T_ph) )

eq = eq0 & eq1
dt = 1e-17
steps = 10000
for step in range(steps):
    T_e.updateOld()
    T_ph.updateOld()
    print('S', A_r)
    res = 1e100
    dt *= 1.001
while res > 1:
        res = eq.sweep(dt=dt, underRelaxation=0.5)
    t.setValue(t + dt)
```

BIBLIOGRAPHY

[1] T. Koyanagi *et al.*, “Recent progress in the development of SiC composites for nuclear fusion applications,” *Journal of Nuclear Materials*, vol. 511. pp. 544–555, 2018, doi: 10.1016/j.jnucmat.2018.06.017.

[2] K. Noborio, Y. Yamamoto, Y. Takeuchi, T. Hinoki, and S. Konishi, “Development of high temperature SiC/SiC composite intermediate heat exchanger for He and LiPb,” *Proc. - Symp. Fusion Eng.*, pp. 1–4, 2009, doi: 10.1109/FUSION.2009.5226504.

[3] W. J. Kim, D. Kim, and J. Y. Park, “Fabrication and material issues for the application of SiC composites to LWR fuel cladding,” *Nucl. Eng. Technol.*, vol. 45, no. 4, pp. 565–572, 2013, doi: 10.5516/NET.07.2012.084.

[4] Y. Katoh and L. L. Snead, “Silicon carbide and its composites for nuclear applications – Historical overview,” *J. Nucl. Mater.*, vol. 526, p. 151849, 2019, doi: 10.1016/j.jnucmat.2019.151849.

[5] “Studying silicon carbide for nuclear fuel cladding - Nuclear Engineering International.” https://www.neimagazine.com/features/featurestudying-silicon-carbide-for-nuclear-fuel-cladding/.

[6] M. Willander, M. Friesel, Q. U. Wahab, and B. Straumal, “Silicon carbide and diamond for high temperature device applications,” *J. Mater. Sci. Mater. Electron.*, vol. 17, no. 1, pp. 1–25, 2006, doi: 10.1007/s10854-005-5137-4.

[7] J. Fan and P. K. Chu, *Silicon Carbide Nanostructures Fabrication, Structure, and Properties*. 2014.

[8] Z.-A. Ren, J. Kato, T. Muranaka, J. Akimitsu, M. Kriener, and Y. Maeno, “Superconductivity in boron-doped SiC,” J. Phys. Soc. Jpn., vol. 76, no. 10, p. 103710, 2007., doi: 10.1143/JPSJ.76.103710.

[9] R. A. Rymzhanov *et al.*, “Insights into different stages of formation of swift heavy ion tracks,” *Nucl. Instruments Methods Phys. Res. Sect. B Beam Interact. with Mater. Atoms*, vol. 473, no. June, pp. 27–42, 2020, doi: 10.1016/j.nimb.2020.04.005.

[10] V. A. Skuratov, “Effects of swift heavy ion irradiation and simulation of fission fragment impact,” no. August, 2012, [Online]. Available: http://indico.ictp.it/event/a11182/session/41/contribution/24/material/0/0.pdf.

[11] P. K. S. Sourav Bhakta, Indra Sulania, S.Ojha, D. Kanjilal, “Swift heavy ion beam stimulated epitaxial recrystallization of Si/SiO2 heterostructure - ScienceDirect,” *Mater. Lett.*, vol. 308, Part, 2021, doi: https://doi.org/10.1016/j.matlet.2021.131153.

[12] J. Jian and J. Sun, “A Review of Recent Progress on Silicon Carbide for Photoelectrochemical Water Splitting,” *Sol. RRL*, vol. 4, no. 7, 2020, doi: 10.1002/solr.202000111.

[13] W. H. Backes, P. A. Bobbert, and van Haeringen W, “Energy-band structure of SiC polytypes by interface matching of electronic wave functions,” Phys. Rev. B Condens. Matter, vol. 49, no. 11, pp. 7564–7568, 1994.

[14] R. Ji, Y. Liu, Y. Zhang, B. Cai, J. Ma, and X. Li, “Influence of dielectric and machining parameters on the process performance for electric discharge milling of SiC ceramic,” *Int. J. Adv. Manuf. Technol.*, vol. 59, no. 1–4, pp. 127–136, 2012, doi: 10.1007/s00170-011-3493-1.

[15] “yole Development.” http://www.yole.fr/index.aspx.

[16] X. W. Zhou and C. H. Tang, “Current status and future development of coated fuel particles for high temperature gas-cooled reactors,” *Prog. Nucl. Energy*, vol. 53, no. 2, pp. 182–188, 2011, doi: 10.1016/j.pnucene.2010.10.003.

[17] O. Baudrand, D. Blanc,T. Bourgois ,E. Ivanov, H. Bonneville, G. Bruna , B. Clément, G. Hache, M. Kissane , R. Meignen , D. Monhardt, G. Nicaise, “Overview of Generation IV (Gen IV) Reactor Designs,” Sep. 2012..

[18] J. J. Powers W. J. Lee F. Venneri L. L. Snead C. K. Jo D. H. Hwang J. H. Chun Y. M. Kim K. A. Terrani, “FULLY CERAMIC MICROENCAPSULATED (FCM) REPLACEMENT FUEL FOR LWRs,” May 2013..

[19] A. Möslang *et al.*, “Towards reduced activation structural materials data for fusion DEMO reactors,” *Nucl. Fusion*, vol. 45, no. 7, pp. 649–655, 2005, doi: 10.1088/0029-5515/45/7/013.

[20] D. Tochio and S. Nakagawa, “Thermal Performance of Intermediate Heat Exchanger during High-Temperature Continuous Operation in HTTR Thermal Performance of Intermediate Heat Exchanger,” vol. 3131, 2012, doi: 10.1080/18811248.2011.9711828.

[21] J. Wrbanek and S. Wrbanek, “Space Radiation and Impact on Instrumentation Technologies,” January 2020.

[22] R. D. and D. M. Duffy, “Modelling Radiation Effects in Solids with Two-Temperature Molecular Dynamics,” *Nucl. Eng. Des.*, vol. 113, no. 2, pp. 171–172, 1989, doi: 10.1016/0029-5493(89)90068-x.

[23] L. M. Wang *et al.*, “Irradiation-induced nanostructures,” *Mater. Sci. Eng. A*, vol. 286, no. 1, pp. 72–80, 2000, doi: 10.1016/s0921-5093(00)00677-8.

[24] K. Nordlund *et al.*, “Primary radiation damage: A review of current understanding and models,” *J. Nucl. Mater.*, vol. 512, pp. 450–479, 2018, doi: 10.1016/j.jnucmat.2018.10.027.

[25] Y. Zhang *et al.*, “Competing effects of electronic and nuclear energy loss on microstructural evolution in ionic-covalent materials,” *Nucl. Instruments Methods Phys. Res. Sect. B Beam Interact. with Mater. Atoms*, vol. 327, no. 1, pp. 33–43, 2014, doi: 10.1016/j.nimb.2013.10.095.

[26] R. L. Fleischer, P. B. Price, and R. M. Walker, “Ion explosion spike mechanism for formation of charged-particle tracks in solids,” *J. Appl. Phys.*, vol. 36, no. 11, pp. 3645–3652, 1965, doi: 10.1063/1.1703059.

[27] E. M. Bringa and R. E. Johnson, “Coulomb Explosion and Thermal Spikes,” *Phys. Rev. Lett.*, vol. 88, no. 16, p. 4, 2002, doi: 10.1103/PhysRevLett.88.165501.

[28] C. P. Race, D. R. Mason, and A. P. Sutton, “Electronic excitations and their effect on the interionic forces in simulations of radiation damage in metals,” *J. Phys. Condens. Matter*, vol. 21, no. 11, 2009, doi: 10.1088/0953-8984/21/11/115702.

[29] D. Mu, P. V Sushko, and A. L. Shluger, “Models of triplet self-trapped excitons in SiO 2 , HfO 2 , and HfSiO 4,” vol. 024120, 2012, doi: 10.1103/PhysRevB.85.024120.

[30] Q. Zheng, C. Li, A. Rai, J. H. Leach, D. A. Broido, and D. G. Cahill, “Thermal conductivity of GaN, GaN 71, and SiC from 150 K to 850 K,” *Phys. Rev. Mater.*, vol. 3, no. 1, pp. 1–14, 2019, doi: 10.1103/PhysRevMaterials.3.014601.

[31] M. Yamanaka, H. Daimon, E. Sakuma, S. Misawa, and S. Yoshida, “Temperature dependence of electrical properties of n- and p-type 3C-SiC,” *J. Appl. Phys.*, vol. 61, no. 2, pp. 599–603, 1987, doi: 10.1063/1.338211.

[32] S. Y. Savrasov and D. Y. Savrasov, “Electron-phonon interactions and related physical properties of metals from linear-response theory,” 2008.

[33] M. Calandra and F. Mauri, “Electron-phonon coupling and electron self-energy in electron-doped graphene: Calculation of angular-resolved photoemission spectra,” *Phys. Rev. B - Condens. Matter Mater. Phys.*, vol. 76, no. 20, pp. 1–9, 2007, doi: 10.1103/PhysRevB.76.205411.

[34] P. Aynajian, “Electron-Phonon Interaction in Conventional and Unconventional,” *Max-Planck-Institut*, 2009.

[35] T. Tsuneda, *DFT in Quantum Chemistry*. 2014.

[36] X. Blase, X. Blase, D. Functional, T. Pavarini, and X. Blase, “Introduction to Density Functional Theory To cite this version : HAL Id : hal-03070870 Introduction to Density Functional Theory,” 2020.

[37] V. Sahni, “The Hohenberg-Kohn Theorems and Kohn-Sham Density Functional Theory,” *Quantal Density Funct. Theory*, pp. 99–123, 2004, doi: 10.1007/978-3-662-09624-6_4.

[38] G. Carchini *et al.*, “How theoretical simulations can address the structure and activity of nanoparticles,” *Top. Catal.*, vol. 56, no. 13–14, pp. 1262–1272, 2013, doi: 10.1007/s11244-013-0093-3.

[39] Doyeol Ahn and S.-H. Park, *Engineering Quantum Mechanics*. New Jersey, 2011.

[40] P. Pereyra, *Fundamentals of quantum physics: Textbook for students of science and engineering, 2012th ed. Berlin, Germany: Springer, 2012.* Berlin, Germany: Springer, 2012.

[41] H. Schober, “Symmetry characterization of electrons and lattice excitations,” vol. 00012, pp. 1–37, 2012.

[42] M. El Mliles and Y. El Kouari, “Ab initio study of electron and phonon coupling in silicon,” 2020, doi: 10.1088/1757-899X/948/1/012005.

[43] A. Giri, M. V. Tokina, O. V. Prezhdo, and P. E. Hopkins, “Electron–phonon coupling and related transport properties of metals and intermetallic alloys from first principles,” *Mater. Today Phys.*, vol. 12, p. 100175, 2020, doi: 10.1016/j.mtphys.2019.100175.

[44] W. H. Butler, “Electronic structure and the electron — phonon interaction,” in Treatise on Materials Science & Technology, Elsevier, 1981, pp. 165–222, doi: https://doi.org/10.1016/B978-0-12-341821-0.50009-7

[45] M. Roy, “The Tight Binding Method Background : a hierarchy of methods,” pp. 1–15, 2015.

[46] N. Medvedev and I. Milov, “Electron-phonon coupling in metals at high electronic temperatures,” *Phys. Rev. B*, vol. 102, no. 6, pp. 1–22, 2020, doi: 10.1103/PhysRevB.102.064302.

[47] Z. Lin and L. V Zhigilei, “Electron-phonon coupling and electron heat capacity of metals under conditions of strong electron-phonon nonequilibrium,” pp. 1–17, 2008, doi: 10.1103/PhysRevB.77.075133.

[48] M. Roy, “The Tight Binding Method Background : a hierarchy of methods,” pp. 1–15, 2015.

[49] A. T. Paxton, “An introduction to the tight binding approximation — implementation by diagonalisation,” pp. 1–32.

[50] D. J. Griffiths, *Introduction to Quantum Mechanics*. Cambridge, 2017.

[51] S. Savrasov and D. Savrasov, “Electron-phonon interactions and related physical properties of metals from linear-response theory,” *Phys. Rev. B - Condens. Matter Mater. Phys.*, vol. 54, no. 23, pp. 16487–16501, 1996, doi: 10.1103/PhysRevB.54.16487.

[52] A. Majumdar and P. Reddy, “Role of electron-phonon coupling in thermal conductance of metal-nonmetal interfaces,” *Appl. Phys. Lett.*, vol. 84, no. 23, pp. 4768–4770, 2004, doi: 10.1063/1.1758301.

[53] A. Giri, M. V. Tokina, O. V. Prezhdo, and P. E. Hopkins, “Electron–phonon coupling and related transport properties of metals and intermetallic alloys from first principles,” *Mater. Today Phys.*, vol. 12, p. 100175, 2020, doi: 10.1016/j.mtphys.2019.100175.

[54] F. Staub, U. Rau, and T. Kirchartz, “Statistics of the Auger Recombination of Electrons and Holes via Defect Levels in the Band Gap Application to Lead-Halide Perovskites,” 2018, doi: 10.1021/acsomega.8b00962.

[55] F. Wang, G. Dukovic, E. Knoesel, L. E. Brus, and T. F. Heinz, “Observation of rapid Auger recombination in optically excited semiconducting carbon nanotubes,” vol. 241403, pp. 1–4, 2004, doi: 10.1103/PhysRevB.70.241403.

[56] A. You, M. A. Y. Be, and I. In, “Auger recombination in intrinsic GaAs Auger recombination,” vol. 55, no. June 1998, pp. 4–7, 2007.

VITA

Salah Abdul-Rahman Alsmairat was born in Jordan in 1979. He earned his BSc in applied physics from Jordan University of Science and Technology in 2002. In 2005 he was admitted to the European Master in Nuclear Applications (EMiNA) at Aachen University of Science and Technology (Aachen, Germany) and graduated in 2008. After a couple of years of teaching physics and science in high schools, he joined the academic staff of King Abdul Aziz University in Jeddah-Saudi Arabia in 2011 as a lecturer and radiation safety officer in the nuclear engineering department. During his work at King Abdul Aziz University, he taught some courses at the undergraduate level in addition to supervising the laboratories in the department and conducted research on neutron back diffusion imaging. In January 2016, Salah started his Ph.D. at Missouri University of Science and Technology in Nuclear Engineering. He studied the electron-phonon coupling in 3C-SiC using *ab-initio* methods. In December 2021 Salah defended his dissertation successfully. He received his Ph.D. in Nuclear Engineering from Missouri University of Science and Technology in May 2022.